

# Stabilization of the Orthorhombic Phase in $\text{Hf}_{0.5}\text{Zr}_{0.5}\text{O}_2$ Nanoparticles by Oxygen Vacancies

Yuri O. Zagorodniy<sup>1</sup>, Eugene A. Eliseev<sup>1\*</sup>, Valentin V. Laguta<sup>1,2</sup>, Petr Jiricek<sup>2</sup>, Jana Houdkova<sup>2</sup>, Lesya D. Demchenko<sup>3,4</sup>, Oksana V. Leshchenko<sup>1</sup>, Victor N. Pavlikov<sup>1</sup>, Lesya P. Yurchenko<sup>1</sup>, Anna O. Diachenko<sup>5</sup>, Michail D. Volnyanskii<sup>5</sup>, Myroslav V. Karpets<sup>4</sup>, Mikhail P. Trubitsyn<sup>2,5†</sup>, Dean R. Evans<sup>6‡</sup>, and Anna N. Morozovska<sup>7§</sup>

<sup>1</sup> Frantsevich Institute for Problems in Materials Science of the National Academy of Sciences of Ukraine, 3, str. Omeliana Pritsaka, 03142 Kyiv, Ukraine

<sup>2</sup> Institute of Physics of the Czech Academy of Sciences, Na Slovance 1999/2, 18200 Prague 8, Czech Republic

<sup>3</sup> Stockholm University, Department of Chemistry, Sweden

<sup>4</sup> Ye. O. Paton Institute of Materials Science and Welding, National Technical University of Ukraine “Igor Sikorsky Kyiv Polytechnic Institute”, 37, Beresteisky Avenue, Kyiv, Ukraine, 03056

<sup>5</sup> Oles Honchar Dnipro National University, 72, Nauky Avenue, 49000 Dnipro, Ukraine

<sup>6</sup> Zone 5 Technologies, Special Projects, San Luis Obispo CA 93401, USA

<sup>7</sup> Institute of Physics of the National Academy of Sciences of Ukraine, 46, Nauky Avenue, 03028 Kyiv, Ukraine

## Abstract

In this work we study the stabilization of the o-phase in small  $\text{Hf}_{0.5}\text{Zr}_{0.5}\text{O}_2$  nanoparticles (the average size 7 nm) annealed in air and in the  $\text{CO}+\text{CO}_2$  ambient. Concentration of the oxygen vacancies, which is determined by annealing conditions, was estimated from the electron paramagnetic resonance spectra and X-ray photoelectron spectroscopy. The fraction of the orthorhombic phase that was controlled by the X-ray diffraction and nuclear magnetic resonance, depends on the concentration of oxygen vacancies, which are defined by annealing conditions. Phenomenological calculations based on Landau-Ginzburg-Devonshire theory confirm that the chemical strains induced by oxygen vacancies can stabilize the orthorhombic phase with polar and antipolar long-range ordering in small hafnia-zirconia nanoparticles.

---

\*Corresponding author, e-mail [eugene.a.eliseev@gmail.com](mailto:eugene.a.eliseev@gmail.com)

† Corresponding author, e-mail: [trubitsyn\\_m@ua.fm](mailto:trubitsyn_m@ua.fm)

‡ Corresponding author, e-mail: [deanevans@zone5tech.com](mailto:deanevans@zone5tech.com)

§Corresponding author, e-mail [anna.n.morozovska@gmail.com](mailto:anna.n.morozovska@gmail.com)

## I. INTRODUCTION

The discovery of ferroelectricity in thin films of binary oxides such as  $\text{HfO}_2$  and  $\text{ZrO}_2$  [1, 2, 3] made these materials as highly promising candidates for non-volatile memory devices and integrated layered capacitors [4, 5, 6]. Unlike perovskite ferroelectrics, which suffer from poor compatibility with silicon technologies due to substantial lattice mismatches and the formation of interfacial dead layers that degrade their ferroelectric response,  $(\text{Hf,Zr})\text{O}_2$  thin films are free from these deficiencies and thus are successfully used as gate dielectrics in field-effect transistors. Their chemical stability and full compatibility with complementary metal-oxide-semiconductor (CMOS) processes make them particularly attractive for modern microelectronic applications.

The ferroelectric (FE) properties of  $(\text{Hf,Zr})\text{O}_2$  thin films are associated with the formation of polar orthorhombic phase (o-phase) with the non-centrosymmetric space group  $Pca2_1$ . In contrast, bulk  $\text{HfO}_2$  and  $\text{ZrO}_2$ , are nonpolar centrosymmetric materials. At room temperature and normal pressure, both  $\text{HfO}_2$  and  $\text{ZrO}_2$ , which are structurally equivalent, stabilize in the monoclinic phase (m-phase) with the space group  $P2_1/c$ . With increasing temperature, this phase undergoes a transformation to the tetragonal phase (t-phase) with the space group  $P4_2/nmc$ , followed by a transition to the cubic phase (c-phase) with the space group  $Fm3m$  [7, 8]. Under high-pressures, two additional nonpolar o-phases (o-I and o-II) with the space groups  $Pbca$  and  $Pnma$  can be stable [9, 10].

Formation of the FE o-phase was revealed for the first time in 9-nm  $(\text{Hf,Zr})\text{O}_2$  films covered by TiN electrodes [1]. In this experiment, undoped  $\text{HfO}_2$  films had monoclinic symmetry and paraelectric properties,  $\text{ZrO}_2$  films had tetragonal symmetry and anti-ferroelectric properties, while  $(\text{Hf,Zr})\text{O}_2$  thin films demonstrated distinct ferroelectric properties, at that the maximal remanent polarization was observed in  $\text{Hf}_{0.5}\text{Zr}_{0.5}\text{O}_2$  films. It was found later that the stabilization of the FE o-phase in  $\text{HfO}_2$  thin films can be achieved by doping with Si [11], Y [12] or Al [13]. Unlike thin films, bulk materials never undergo a transition to the FE o-phase under doping, temperature, pressure, or other external factors.

The formation of the FE phase in  $(\text{Hf,Zr})\text{O}_2$  thin films can be attributed to several factors, including elastic strains arising from deposition on substrates with different lattice parameters [14, 15, 16], changes in the electronic structure due to doping, lattice distortions caused by the formation of oxygen vacancies [17, 18], size effects [19], as well as due to the interplay of all these mechanisms.

The important role of oxygen vacancies in stabilization of the FE o-phase in thin films and nanoparticles has been confirmed by numerous experimental [20, 21] and theoretical [22] studies. In particular, it was demonstrated in experimental works [2, 20] that the ferroelectric properties of undoped 15 nm thick  $\text{HfO}_2$  films, deposited on Pt, TiN, and Si substrates and annealed in a nitrogen ambient, are determined by the concentration of oxygen vacancies, as follows from the X-ray photoelectron spectroscopy analysis. It was later shown experimentally that oxygen-deficient  $\text{Hf}_x\text{Zr}_{1-x}\text{O}_{2-y}$  nanoparticles, which contain a large fraction of o-phases due to the annealing in  $\text{CO}+\text{CO}_2$  ambient [23,

24], can exhibit ferroelectric-like properties, such as a colossal dielectric response over a wide frequency range [25], as well as demonstrate resistive switching and pronounced charge accumulation [26].

Also, it was shown theoretically [22] that the influence of vacancies on the stabilization of the FE o-phase arises from the formation of elastic dipoles around point defects, which leads to the local breaking of the inversion symmetry. Furthermore density functional theory (DFT) calculations, performed in Ref. [21], confirmed the influence of oxygen vacancies on the phase stability of HfO<sub>2</sub> and revealed that the FE o-phase becomes energetically more favorable than the m-phase, although it remains less favorable than the tetragonal and cubic phases. However, the physical mechanisms governing the stabilization of the FE phase are not sufficiently studied.

In this work we study the stabilization of the o-phase in the (Hf,Zr)O<sub>2</sub> nanoparticles with different concentrations of oxygen vacancies. The choice of the nanoparticles is due to the desire to get rid of the possible influence of the substrate, thus leaving only size effect and the effects connected with the concentration of defects associated with the vacancies. Concentration of the oxygen vacancies was estimated by the electron paramagnetic resonance (EPR) and X-ray photoelectron spectroscopy (XPS); the phase composition was estimated by the X-ray diffraction (XRD) and nuclear magnetic resonance (NMR). Phenomenological calculations based on Landau-Ginzburg-Devonshire theory were performed to confirm the stabilization of the FE o-phase by the chemical strains induced by oxygen vacancies.

## II. EXPERIMENTAL RESULTS AND DISCUSSION

### A. Samples and Experimental Techniques

To study how oxygen vacancies affect the emergence of possibly ferroelectric o-phase, we prepared Hf<sub>0.5</sub>Zr<sub>0.5</sub>O<sub>2</sub> nanoparticles by the solid-state organonitrate synthesis. The process employed aqueous mixtures of zirconium and hafnium nitrate salts (ZrO(NO<sub>3</sub>)<sub>2</sub>·2H<sub>2</sub>O and Hf(NO<sub>3</sub>)<sub>2</sub>·2H<sub>2</sub>O), dissolved in distilled water at concentrations not exceeding 5 – 10% (for methodological details, see Refs. [27, 28]). The Hf<sub>0.5</sub>Zr<sub>0.5</sub>O<sub>2</sub> nanoparticles in the sample N1 were annealed in air at 700 °C for 6 hours. The sample N2 consists of Hf<sub>0.5</sub>Zr<sub>0.5</sub>O<sub>2</sub> nanoparticles annealed at 500°C for 6 hours in the CO + CO<sub>2</sub> ambient to increase strongly the concentration of oxygen vacancies.

Composite materials were prepared from both types of the Hf<sub>0.5</sub>Zr<sub>0.5</sub>O nanoparticles embedded in the PVDF polymer matrix. The samples were prepared from pre-compressed (10 MPa) composites in the form of irregularly shaped plates with linear dimensions of 5 – 8 mm and a thickness of about 0.5 – 0.8 mm. The Hf<sub>0.5</sub>Zr<sub>0.5</sub>O<sub>2</sub> powder (taken from N1 or N2 sample) occupied approximately 12.5 vol. % of the total composites volume. Silver electrodes were deposited on the faces of the samples. The electrical properties of Hf<sub>0.5</sub>Zr<sub>0.5</sub>O<sub>2</sub> – PVDF composites were measured in the AC field ( $f \approx 10^2 - 10^6$  Hz) using a Keysight E4980AL LCR meter. Measurements were performed from room temperature up to ~440 K,

above which the PVDF-based composites significantly softened due to heating, and the correct measurements became impossible.

The X-ray photoelectron spectra (XPS) were measured by the AXIS Supra photoelectron spectrometer using monochromatized Al K $\alpha$  radiation (1486.6 eV, 300 W, area analyzed – 0.7 $\times$ 0.3 mm<sup>2</sup>). A source of gas cluster ions was used to remove contaminants from the surface. To minimize the damage of the sample surface due to interaction with high-energy ions, the ion source operated in the cluster mode (the energy of the primary cluster ion was 5 keV, and the number of argon atoms in the cluster was 2000). This mode of the ion source reduces significantly the surface damage of the samples. The irradiation time with primary cluster ions was 5 minutes. Photoelectron lines were recorded before and after the etching process. The main peak of the C 1s spectrum, corresponding to carbon contamination (C–C) was set at 284.5 eV.

The NMR spectra were collected at room temperature using Bruker (Avance II) 9.4 T commercial spectrometer. Extremely broad <sup>91</sup>Zr spectra were obtained by stepping the spectrometer frequency through the spectrum and acquiring the spin-echoes by the conventional 90x- $\tau$  and 90y- $\tau$  spin echo pulse sequence. The spin-echo delay time  $\tau$  was 20  $\mu$ s and the repetition delay time between the scans was 0.1 s. Four-phase “exorcycle” phase sequence (xx, xy, x-x, x-y) was used to form echoes with minimal distortions due to antiechoes, ill-refocused signals, and piezoresonances [29]. The length of the  $\pi/2$  pulse was  $t_{\pi/2} = 2\mu$ s. Individual echoes were Fourier transformed and then superimposed in the frequency domain. Spectral simulations were performed using TopSpin software package and the MRSimulator program [30].

EPR spectra were recorded using a Bruker Elexsys E580 spectrometer operating in the X-band (9.8 GHz) with a magnetic field modulation of 100 kHz. The effective g-values were determined according to the relation  $g_{\text{eff}} = h\nu / (\mu_B H_r)$ , where  $h$  denotes Planck’s constant,  $\nu$  the microwave frequency,  $\mu_B$  the Bohr magneton, and  $H_r$  the resonance field. Spectral simulations and parameter fitting were carried out with the EasySpin software package [31].

## B. SEM, TEM and EDS Results

According to the scanning electron microscopy (SEM) analysis (see **Fig. S1** in the Supplement), the samples N1 – N2 are homogenous and consist of particles’ clusters with the average size of about 65 nm. The electron dispersion spectra (EDS) analysis confirmed that the constituent elements (Hf, Zr, and O) are uniformly distributed in the Hf<sub>0.5</sub>Zr<sub>0.5</sub>O<sub>2</sub> nanoparticles, forming a solid solution (see **Fig. S2** in the Supplement). At the same time, the appearance of the Debye-Scherrer rings and the images obtained by the transmission electron microscopy (TEM) show that the Hf<sub>0.5</sub>Zr<sub>0.5</sub>O<sub>2</sub> nanoparticles have individual sizes around 7 nm and high crystallinity degree (see **Fig. 1**).

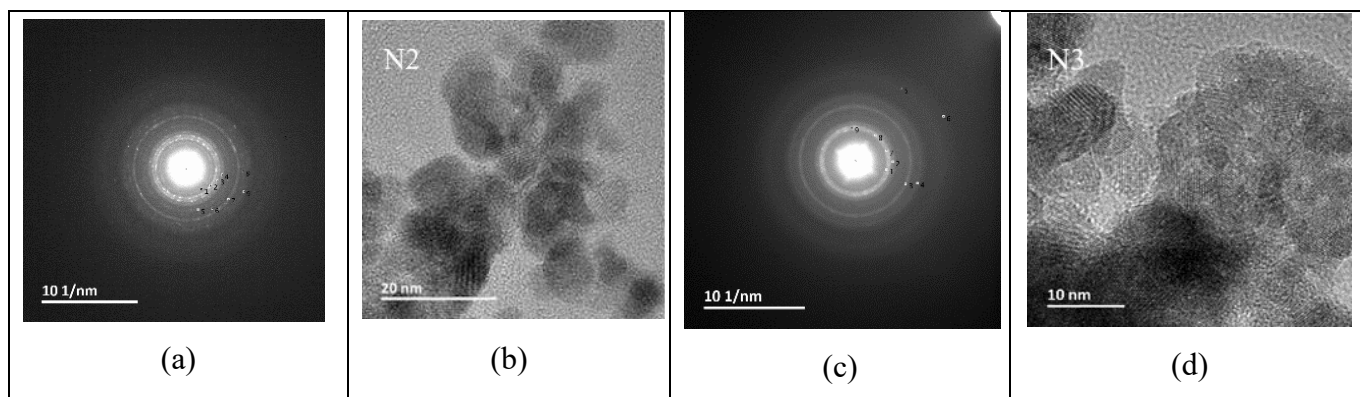


**Figure 1.** TEM images of  $\text{Hf}_{0.5}\text{Zr}_{0.5}\text{O}_2$  nanoparticles annealed in air (a, b) and in the  $\text{CO} + \text{CO}_2$  ambient (c, d).

The X-ray diffraction (XRD) measurements of the samples are presented in **Fig. S3** (see Supplement). Despite the high crystallinity of the nanoparticles, their XRD spectra are characterized by broad diffraction lines arising from significant surface effects, thereby complicating the analysis. While the spectrum of the monoclinic phase differs significantly from other possible phases, the spectra of the tetragonal and orthorhombic phases are very difficult to distinguish from each other using X-ray diffraction spectra. The three orthorhombic phases are even more difficult to distinguish, as they have almost identical cation arrangement and differ only in the positions of the oxygen atoms [32].

Based on the full-profile analysis of the XRD spectra, the  $\text{Hf}_{0.5}\text{Zr}_{0.5}\text{O}_2$  nanopowders annealed in air (sample N1) predominantly display a coexistence of the m-phase (63.54 wt. %) and the o-phase (36.46 wt. %). The sample N2, which consists of the  $\text{Hf}_{0.5}\text{Zr}_{0.5}\text{O}_2$  nanopowders annealed in the  $\text{CO} + \text{CO}_2$  ambient, reveals the purely o-phase (100 wt. %). To achieve a clearer distinction between the tetragonal and orthorhombic phases, nuclear magnetic resonance (NMR) measurements were performed.

Distinguishing among the three orthorhombic phases is particularly challenging. However, the mechanism of formation of the orthorhombic phase under the influence of oxygen vacancies promotes the formation of the polar phase. Thus, the polar phase arises from the displacement of one type of oxygen atoms along the axis Z. Displacement in the opposite direction can also induce the polar phase with an opposite polarity. The unit cell of the nonpolar phase can be imagined as consisting of two coupled polar cells, distinguished by oxygen displacements in opposite directions [33]. Considering that the orthorhombic phase arises from elastic strains due to the lattice displacements in the presence of oxygen vacancies [22], it is reasonable to assume that the oxygen atoms shift in the same direction in this case, which gives rise to the ferroelectric phase.

### C. X-ray Photoelectron Spectroscopy Results

To study the variations in the chemical composition and valence states of surface species depending on the synthesis conditions, the samples were examined by the X-ray photoelectron

spectroscopy (XPS). To distinguish between the possible defects and surface contamination, the Hf 4f, Zr 3d and O 1s XPS spectra were obtained for as-prepared samples and the samples after etching their surface for 300 seconds with argon ions.

The Hf 4f and Zr 3d XPS spectra consist of two main lines corresponding to the spin-orbit splitting of their 4f and 3d electrons. Fitting each component of the Hf 4f doublet by Gaussian lines yields binding energies of 18.2 and 16.5 eV ( $\pm 0.1$  eV) for Hf 4f<sub>5/2</sub> and Hf 4f<sub>7/2</sub>, respectively, which corresponds to the Hf-O bond, where Hf is in the oxidation state +4. Fitting the Zr 3d doublet gives 182.1 and 184.5 eV ( $\pm 0.1$  eV) for 3d<sub>5/2</sub> and 3d<sub>3/2</sub>, corresponding to Zr<sup>4+</sup> in ZrO<sub>2</sub>. The positions of these peaks are virtually identical for all samples. Any visible shoulder with a lower binding energy that could correspond to a metal in the oxidation state of +3 is absent in the XPS spectra.

The main difference in the spectra is the shoulder with a higher binding energy, whose intensity depends on the samples preparation conditions and decreases substantially after etching the sample surface. **Figure 2** shows the Hf 4f and Zr 3d XPS spectra of Hf<sub>0.5</sub>Zr<sub>0.5</sub>O<sub>2</sub> annealed in CO+CO<sub>2</sub> ambient, which has the maximal intensity of the shoulder in both Hf and Zr XPS spectra. The high-energy shoulder in the spectra of transition metals, Hf and Zr, is usually associated with shake-up satellites [34, 35]. Their intensity depends on the degree of covalence of the chemical bond formed in this case by the metal atoms with the functional groups present at the surface (mainly with oxygen); also, it can be due to surface contamination during the synthesis process. Partial removal of surface contaminants and weakly bound groups reduces significantly the intensity of this peak.

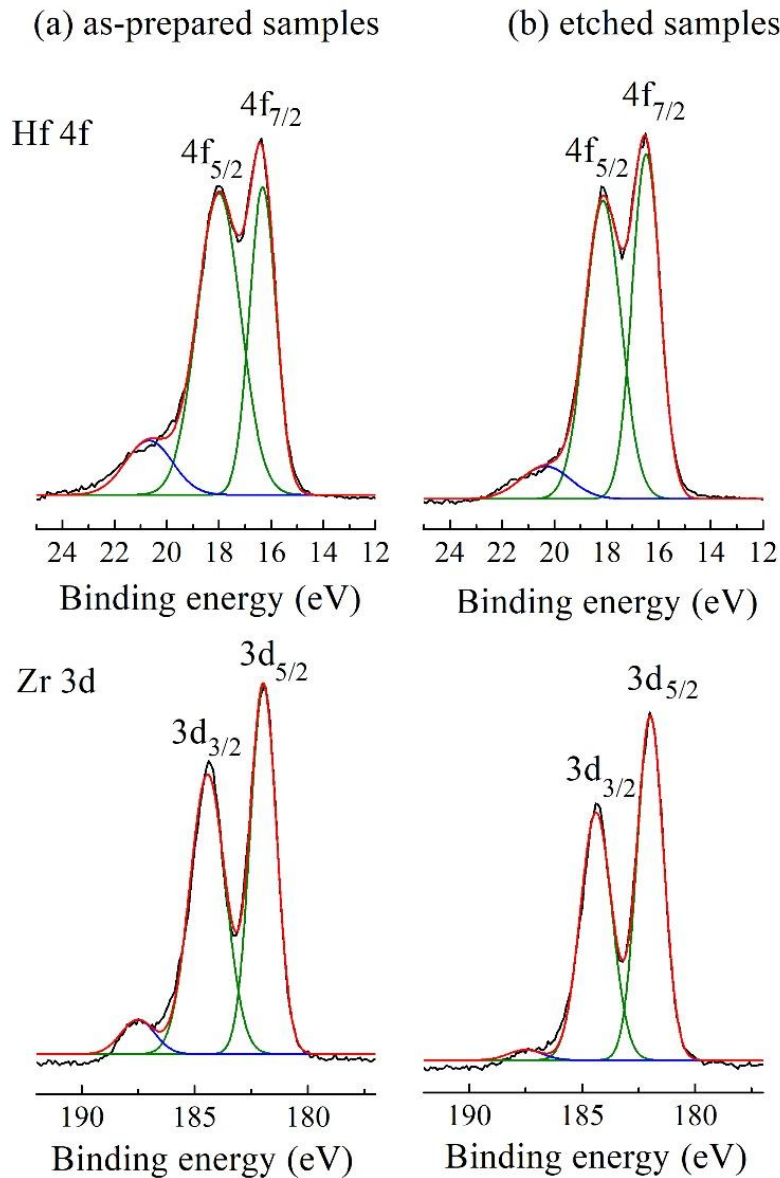


**Figure 2.** Hf 4f and Zr 3d XPS spectra of the  $\text{Hf}_{0.5}\text{Zr}_{0.5}\text{O}_2$  nanoparticles annealed in  $\text{CO}+\text{CO}_2$  ambient (sample N2). The column **(a)** corresponds to as-prepared samples and the column **(b)** – to the samples after etching of their surface during 300 s. Black curves are experimentally measured spectra, red curves are their fitting by three Gaussians shown by the green and blue colors.

To obtain more details about the formation of chemical bonds by oxygen atoms and, possibly, to track the formation of oxygen vacancies, a detailed study of the high resolution O1s XPS spectra was performed (see **Fig. 3**). The O1s XPS spectra of the as-prepared samples (**Fig. 3**, column **(a)**) shows a highly asymmetric peak, which can be decomposed into three Gaussian lines with binding energies of about 530, 531.5 and 532.2 – 533.8 eV. They are designated as I, II, III in **Fig. 3**. As can be seen from the figure, the shape of the O1s line depends significantly on the synthesis conditions. The change in the number of defects presumably induced in the samples (depending on the synthesis conditions) is accompanied by a change in the asymmetry of the spectral line, which is manifested in a greater relative

intensity of the peaks II and III. The binding energies of 1s electrons for all lines obtained from the spectra decomposition on Gaussians, as well as the contribution of individual peaks, are presented in **Table 1**, which also provides the contribution of the orthorhombic phase in the studied samples, determined from the X-ray diffraction spectra.

O 1s

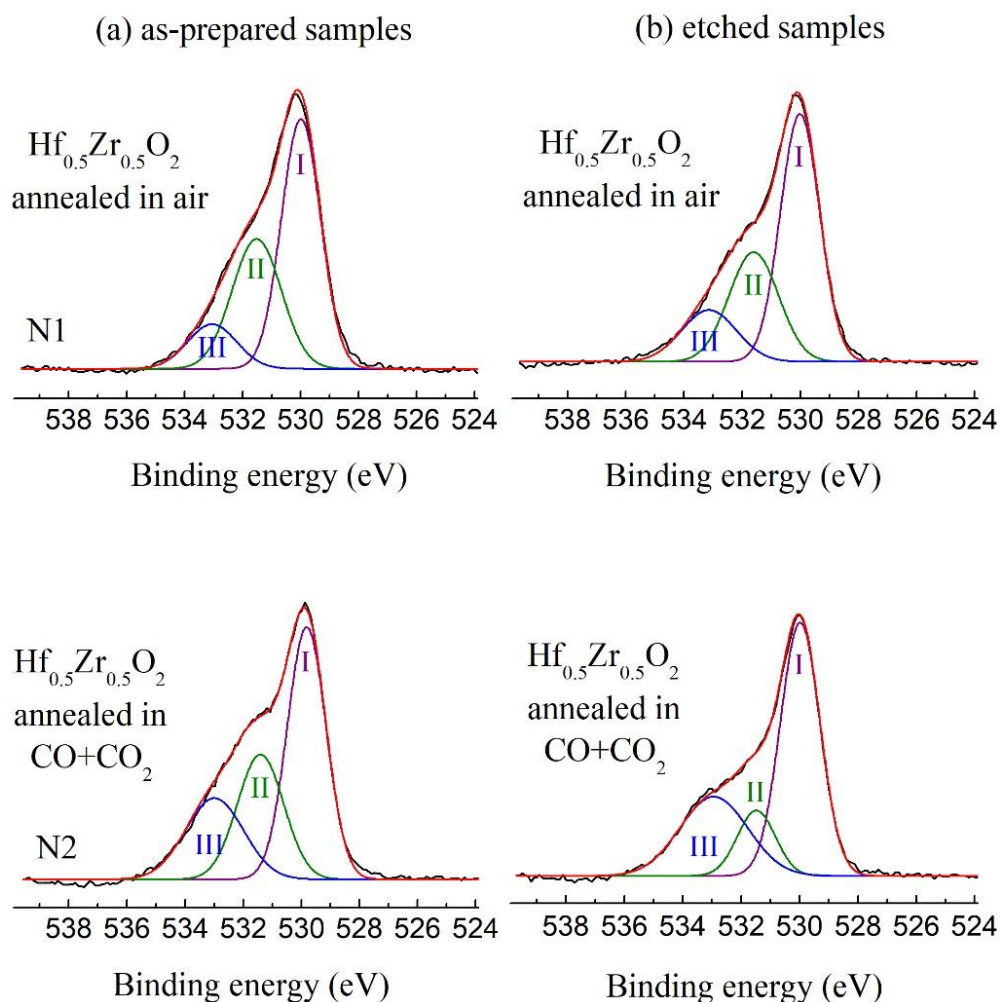


**Figure 3.** O1s XPS spectra of the studied as-prepared  $\text{Hf}_{0.5}\text{Zr}_{0.5}\text{O}_2$  samples (column **(a)**) and the samples after etching their surface during 300s (column **(b)**). Black curves are experimentally measured spectra, red curves are their fitting by three Gaussians shown by the violet, green and blue colors. The preparation conditions of the samples are described in **Table 1**.

**Table 1.** Preparation conditions of the  $\text{Hf}_{0.5}\text{Zr}_{0.5}\text{O}_2$  nanopowders, the binding energy and the peak area obtained in the result of the Gaussian decomposition of O1s XPS spectra, and the fraction of the o-phase in the studied samples

Nanopowder samples	Binding Energy (eV)	Peak Area (%)	Fraction of the orthorhombic phase
--------------------	---------------------	---------------	------------------------------------

									(wt. %, determined from XRD)
			I	II	III	I	II	III	
N1	Hf <sub>0.5</sub> Zr <sub>0.5</sub> O <sub>2</sub> annealed in air	As prepared	530	531.5	533.1	53	35	12	36
		After etching	530	531.8	533.1	54	30	16	
N2	Hf <sub>0.5</sub> Zr <sub>0.5</sub> O <sub>2</sub> annealed in CO+CO <sub>2</sub>	As prepared	529.8	531.4	533	48	29	23	100
		After etching	530	531.5	532.9	56	14	30	

The most intense peak I in these compounds corresponds to the line with a binding energy of about 530 eV and can be assigned to lattice oxygen, which has similar values in the HfO<sub>2</sub> and ZrO<sub>2</sub> [36, 37], where the Hf and Zr ions have an oxidation state of +4 and oxygen vacancies or other defects are absent. Peaks II and III, by their position, can belong to hydroxyl groups or various carbon groups, such as physically adsorbed CO<sub>2</sub> molecules, carbonates formed in result of the interaction of CO with oxygen at the surface, as well as defects of the C-O-*Me* type, where the metal *Me* refers to hafnium or zirconium. These defects may be present in the Hf<sub>0.5</sub>Zr<sub>0.5</sub>O<sub>2</sub> samples due to the synthesis conditions. However, there are many studies in which the O1s peaks with higher binding energy are considered to be characteristic of oxygen vacancies present in the samples [38, 39, 40, 41, 42, 43]. In this case, the peak II refers to O1s from oxygen-deficient regions, and the peak III refers to the surface vacancies filled by OH groups. Several explanations have been proposed for the sensitivity of O1s spectra to oxygen vacancies, such as the increase in the binding energy of 1s electrons of oxygen atoms located near trivalent metal ions being due to a decrease in the electron density on neighboring oxygen atoms.

While this approach is widely accepted in the literature, the attribution of this O1s peak to the oxygen deficient regions has also attracted serious criticism. One of the arguments is that water molecules absorbed from the surrounding atmosphere immediately oxidize the metal oxide with oxygen vacancies presented in their structure. This leads to the healing of the surface oxygen vacancy and the appearance of the O1s signals in the region of 531.5 – 533 eV due to absorbed water and hydroxyl groups formed in result of dissociation of adsorbed water [44]. Also, the DFT calculations for different metal oxides approve that oxygen vacancies have very small effect on the O1s binding energies of neighboring oxygen atoms, while the OH groups shift the core levels of the lattice oxygen for more than 2 eV [45].

Despite the controversy of assignment of the oxygen vacancies by the O1s peak and the lack of a reliable physical basis for the proposed explanations, there is a clear correlation between the number of vacancies intentionally induced in the sample and the shape of the XPS line. The samples studied in this work, according to their synthesis conditions, should have different numbers of oxygen vacancies in their structure. The presence of vacancies, as well as the presence of Hf<sup>3+</sup> and Zr<sup>3+</sup> ions, which were not confirmed by the Hf 4f and Zr 3d XPS peaks, is also reliably confirmed by the EPR studies (see next section), which is a volumetric technique, whereas XPS probes nanoparticles located within the sample surface layer of about 5-10 nm, which are influenced by the ambient atmosphere.

The relative contribution of lines I–III changes significantly in the XPS spectra of the etched samples (**Fig. 3**, column **b**). For both samples, a sharp decrease in the intensity of the peak II is observed (see **Table 1**), which allows us to conclude that this peak includes signals from the contaminants of the surface as well as from weakly bounded molecules on the sample surface. Meanwhile, the relative intensity of the peak III with higher binding energy increases and reaches the maximum for the  $\text{Hf}_{0.5}\text{Zr}_{0.5}\text{O}_2$  sample annealed in the  $\text{CO}+\text{CO}_2$  ambient. This result can be explained by the role of oxygen vacancies, which act as active surface centers and promote the absorption of water molecules with subsequent dissociation some of them to the OH groups depending on the number of electrons (from 0 to 2) captured by the vacancy. This also implies that water and OH groups adsorbed by the sites of oxygen vacancies are bound to the surface more strongly. It can be used as a tool for a rough quantitative estimate of the number of vacancies. However, it is impossible to obtain an accurate estimation, since water is adsorbed not only by the sites of oxygen vacancies.

The relative intensity of the peak III in the sample  $\text{Hf}_{0.5}\text{Zr}_{0.5}\text{O}_2$  annealed in the  $\text{CO}+\text{CO}_2$  ambient is approximately twice as high as that in all other samples. At the same time this sample has the 100% o-phase content, as follows from the XRD data, which confirms the correctness of such assignment and the influence of the oxygen vacancies on the formation of the o-phase in the studied samples.

We tried to estimate the increase in the vacancy concentration at the surface of a sample annealed in  $\text{CO}+\text{CO}_2$ , which is a 100 % orthorhombic phase, compared to a sample annealed in air. This was done by assuming that OH groups and water settle in the vacancies sites (at the surface), producing their own peak (at a different position in the spectrum from the main oxygen). An increase in its intensity directly indicates an increase in the number of vacancies. By this way we estimated that the  $\text{Hf}_{0.5}\text{Zr}_{0.5}\text{O}_2$  sample  $\text{N}_2$  annealed in  $\text{CO}+\text{CO}_2$  ambient has 10 – 15% of oxygen vacancies.

#### **D. Electron Paramagnetic Resonance Spectroscopy**

The electron paramagnetic resonance (EPR) is a powerful technique for characterizing defects in the studied structures, whose appearance is associated with the presence of uncompensated electron spins. Such defects include oxygen vacancies with a single trapped electron. Moreover, the formation of oxygen vacancies is accompanied by a reduction in the valence state of neighboring Hf or Zr cations. This reduction can lead to the presence of uncompensated 5d or 4d electrons on hafnium and zirconium, giving rise to EPR signals corresponding to  $\text{Hf}^{3+}$  and  $\text{Zr}^{3+}$  ions. These spectral features are well documented in the literature [46, 47] and can be effectively used to estimate the concentration of oxygen vacancies in the investigated samples.

EPR spectra of  $\text{Hf}_{0.5}\text{Zr}_{0.5}\text{O}_2$  nanoparticles without intentional oxygen vacancy formation have been analyzed in Ref. [48]. In the present work, the spectra of the hafnia-zirconia compounds show significant differences only in the samples containing varying concentrations of oxygen vacancies and

other synthesis-induced defects. **Figure 4** presents the spectra of  $\text{Hf}_{0.5}\text{Zr}_{0.5}\text{O}_2$  nanoparticles annealed in air (the sample N1) and in a  $\text{CO}+\text{CO}_2$  ambient (the sample N2).

The effective  $g$  factors were calculated using the equation,  $g_{\text{ef}} = h\nu/\mu_{\text{B}}H_r$ , where  $h$  is Planck's constant,  $\nu$  is the operating frequency,  $\mu_{\text{B}}$  is Bohr magneton, and  $H_r$  is a magnetic resonant field. The intensities of the lines presented in **Figure 4** are not normalized to the number of spins; instead they are chosen for the convenience of presenting the spectra in one figure.

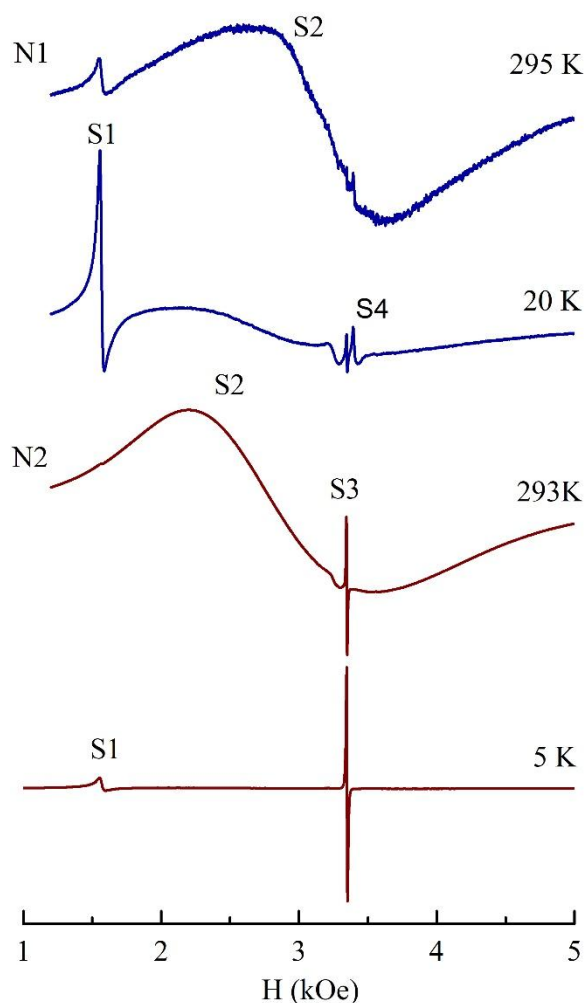


**Figure 4.** EPR spectra of  $\text{Hf}_{0.5}\text{Zr}_{0.5}\text{O}_2$  nanopowders annealed in air (sample N1) and in  $\text{CO}+\text{CO}_2$  atmosphere (sample N2) recorded at two different temperatures.

The EPR spectra of the studied compounds generally exhibit four lines of varying intensity, depending on the sample and the measurement temperature. Line S1, with a  $g$ -factor of approximately 4.3, corresponds to uncontrolled  $\text{Fe}^{3+}$  impurities present in all samples. The broad line S2, with a  $g$ -factor in the range of 2.0 – 2.4, is attributed to paramagnetic ions with uncompensated electron spins. These ions form clusters where dipole–dipole and exchange interactions between individual spins contribute to the observed line broadening. The presence of this line in both types of samples, together with the high

density of oxygen vacancies in the surface layer of nanoparticles annealed in air and in CO+CO<sub>2</sub>, suggests that S2 is primarily associated with clusters formed in the surface region.

The sharp line S3, with a g-factor of 2.0031, appears in all compounds but shows markedly higher intensity in the sample annealed in CO+CO<sub>2</sub>. This line can be attributed to oxygen vacancies containing a trapped electron [46], as well as to carbon radicals remaining after synthesis. To exclude contributions from organic radicals, whose EPR signals typically saturate at low temperatures, spectra were recorded while gradually lowering the sample temperature. It was observed that the relative intensity of S3 increases significantly upon cooling. **Figure 5** illustrates the spectra at two extreme temperatures. Both samples exhibit partial saturation of the S2 line, whereas the S3 line remains unsaturated and dominates the spectrum of sample N2, which is based on synthesis conditions, is expected to contain a large number of oxygen vacancies. The absence of saturation, together with the narrow linewidth (peak-to-peak width of ~5 G), indicates that exchange interactions between paramagnetic centers are sufficiently strong to produce exchange narrowing, thereby confirming a high concentration of oxygen vacancies in this compound.

At the same time, in the spectrum of sample N1, where the intense S3 line does not dominate, an additional feature S4 is clearly resolved at low temperature. Detailed EPR spectra of both samples, obtained in a narrow range around the S4 feature, are presented in **Fig. 5**. The spectrum of sample N1 recorded at 20 K, in addition to the moderate-intensity S3 line, reveals two additional distinct features: a line with  $g_x = 1.999$ ,  $g_y = 2.008$ , and  $g_z = 2.004$ , which can be attributed to hole-type oxygen centers [49]; and a line with  $g_x = 1.948$ ,  $g_y = 1.975$ , and  $g_z = 1.967$ . The latter, whose theoretical simulation is shown at the bottom of the figure, corresponds to isolated Hf<sup>3+</sup> and Zr<sup>3+</sup> ions [48, 49, 50].

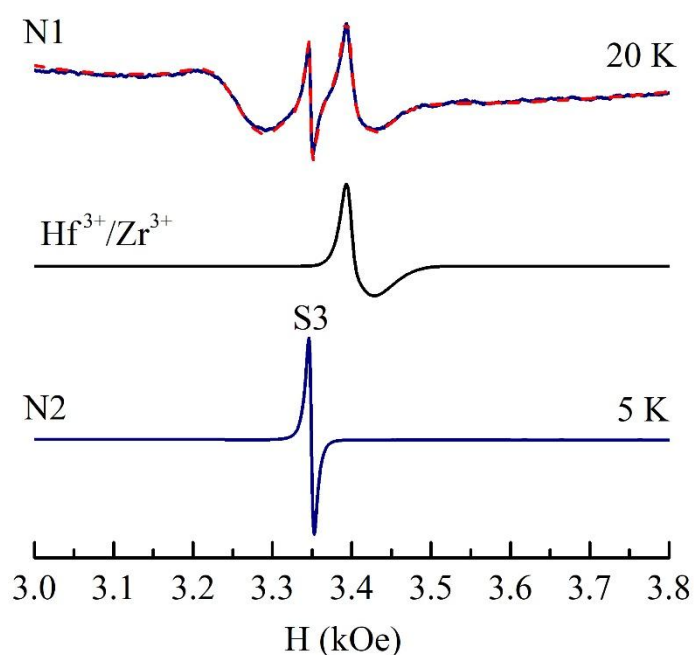


**Figure 5.** Detailed EPR spectra of  $\text{Hf}_{0.5}\text{Zr}_{0.5}\text{O}_2$  nanoparticles annealed in air (the sample N1), obtained at 20 K, and  $\text{Hf}_{0.5}\text{Zr}_{0.5}\text{O}_2$  nanoparticles annealed in  $\text{CO}+\text{CO}_2$  ambient (the sample N2), obtained at 5 K, together with the fitting of the spectrum of the sample N1 (the red dashed line) and the fitting component corresponding to  $\text{Hf}^{3+}$  and  $\text{Zr}^{3+}$  ions.

Thus, the sample N2, which contains a large concentration of oxygen vacancies, intentionally introduced during synthesis, demonstrates the formation of clusters in which the density of paramagnetic ions — such as oxygen vacancies with trapped electrons and  $\text{Hf}^{3+}/\text{Zr}^{3+}$  ions — is sufficient to produce an exchange-narrowed line. This signal dominates the EPR spectra across all temperatures, down to 5 K.

### E. Nuclear Magnetic Resonance Spectra of $^{91}\text{Zr}$

Nuclear magnetic resonance (NMR) spectra provide a powerful method to study the symmetry of the local atomic environment; it is widely used to determine the phase composition of the samples [51, 52]. The most suitable isotope for NMR studies of  $\text{Hf}_{0.5}\text{Zr}_{0.5}\text{O}_2$  nanoparticle is the  $^{91}\text{Zr}$ , which has natural abundance of 11.2%, nuclear spin  $I = 5/2$  and the quadrupole moment  $eQ = -17.6 \text{ fm}^2$ .

As demonstrated in studies of zirconia-based materials [52], the shape of the  $^{91}\text{Zr}$  NMR spectra in zirconium oxides is primarily determined by the quadrupolar interaction of the zirconium nuclei with the electric field gradient (EFG) generated by the surrounding charges. The spin Hamiltonian of the quadrupolar interactions can be expressed as:

$$\mathbf{H}_Q = \frac{C_Q h}{4I(2I-1)} \left[ 3I_z^2 - I^2 + \frac{\eta}{2}(I_+ + I_-) \right], \quad (1)$$

where,  $C_Q = e^2 Q V_{zz} / h$  is the quadrupole coupling constant, proportional to the largest eigenvalue  $V_{zz}$  of the EFG tensor in its principal axes system with  $|V_{zz}| > |V_{xx}| > |V_{yy}|$ , and  $\eta = (V_{xx} - V_{yy}) / V_{zz}$  is the asymmetry parameter of the EFG tensor.

Only the central  $1/2 \leftrightarrow -1/2$  transition, which is affected by the second-order perturbation to the Zeeman interaction, is well resolved in the spectra of powdered samples. The frequency shift of the central transition due to the quadrupole interaction can be presented as:

$$\nu_{1/2}^{(2)} = -\frac{\nu_Q^2}{16\nu_L} \left( I(I+1) - \frac{3}{4} \right) f_\eta(\theta, \varphi), \quad (2)$$

where  $\nu_Q = -\frac{3C_Q}{2I(2I-1)}$ , and the function  $f_\eta(\theta, \varphi)$  depends on the asymmetry of the EFG tensor and on the orientation of its principal axes relative to the external magnetic field [53].

The central transition line in the  $^{91}\text{Zr}$  NMR spectra typically exhibits a width on the order of several hundred kilohertz, even in bulk samples [52, 54]. The higher-order satellite transitions in powdered samples broadened due to the much stronger first-order quadrupolar interaction and the distribution of quadrupolar parameters arising from local structural distortions, which prevents their resolution in the spectra. Nevertheless, the overall shape of the  $^{91}\text{Zr}$  NMR spectra reflects the symmetry

of the crystalline phase, as this determines the local symmetry of the electric field gradient (EFG) at the zirconium nuclei. For example, in a phase with tetragonal symmetry, the zirconium site exhibits  $\eta = 0$  and a quadrupole coupling constant  $C_Q = 19.1$  MHz, whereas in the monoclinic phase  $\eta$  increases slightly to 0.1 [52]. In contrast, specially prepared magnesia-partially stabilized zirconia (MgO-PSZ), containing 45.5% of the orthorhombic phase as confirmed by neutron diffraction, exhibits markedly different parameters:  $C_Q = 17$  MHz and  $\eta = 0.8$ , where the large asymmetry parameter  $\eta$  alters significantly the spectral line shape [52].

The experimental  $^{91}\text{Zr}$  NMR spectrum of  $\text{Hf}_{0.5}\text{Zr}_{0.5}\text{O}_2$  nanoparticles, annealed in  $\text{CO}+\text{CO}_2$  ambient, is presented in the upper part of **Fig. 6**. The best fitting of the spectrum requires two components, reflecting the presence of distinct regions with different distributions of quadrupolar parameters around the zirconium nuclei. Regions in close proximity to defects or nanoparticles surfaces exhibit a broad distribution of quadrupolar parameters, producing a wide line in the spectrum that is well approximated by a Gaussian function (see **Fig. 6(c)**). In contrast, regions with a more moderate distribution of quadrupolar parameters exhibit a distinct local symmetry. Their NMR response can be modeled using Eq.(1) with  $C_Q = 17.8$  MHz and  $\eta = 0.8$  (see **Fig. 6(b)**). These values are in good agreement with those previously reported for the o-phase of MgO-PSZ.

To emphasize the distinction between the orthorhombic and tetragonal phases, the lower part of **Fig. 6** shows a line constructed using the same quadrupole coupling constant  $C_Q$  and other parameters as in line (b), but with  $\eta = 0$ , corresponding to the EFG of zirconium in a tetragonal environment. The pronounced difference in line shapes confirms the correct assignment of the experimental spectrum to the o-phase.

It should be noted that a nearly featureless line of this type is typically observed in disordered materials such as glasses. To describe the distribution of the EFG in disordered or partially disordered systems, the Czjzek or extended Czjzek model is typically employed to construct the corresponding NMR line. The Czjzek model allows to determine the quadrupolar parameters influencing the shape of the NMR spectra in assumption of the Gauss distribution of the EFG values with a zero mean values. On the other hand, the extended Czjzek model assumes that the EFG tensor can be presented as:  $V = V_0 + \varepsilon V_G$ , where  $V_0$  denotes a well-defined contribution arising from the average local symmetry, and  $V_G$  is a Gaussian-distributed random component described by the Czjzek model. The parameter  $\varepsilon$  controls the degree of admixture between the ordered and disordered contributions to the EFG [55, 56].

In this context, inset in **Fig. 6** shows the fit of the experimental spectrum, where the regions preserving average local symmetry are modeled using the extended Czjzek approach. A slightly larger quadrupolar constant is obtained,  $C_Q = 19$  MHz, with the best fitting corresponding to  $\eta = 0.8$ , indicating the orthorhombic symmetry. For comparison, the line shape associated with the tetragonal phase is

characterized by  $C_Q = 19$  MHz and  $\eta = 0$  under the extended Czjzek distribution; it is shown at the bottom of inset in **Fig. 6**.

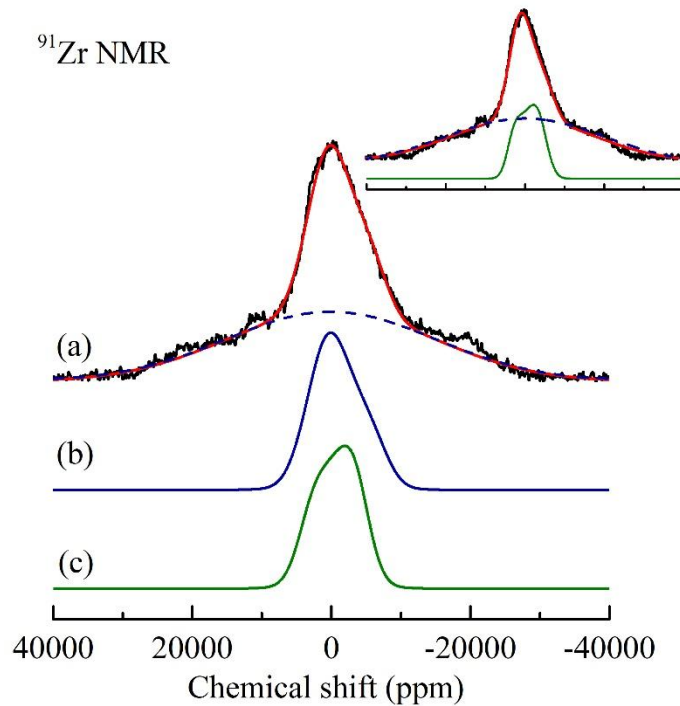


**Figure 6.** (a) Experimental  $^{91}\text{Zr}$  NMR spectrum of  $\text{Hf}_{0.5}\text{Zr}_{0.5}\text{O}_2$  nanoparticles annealed in  $\text{CO}+\text{CO}_2$  ambient together with the best fit, with the dashed line presenting Gaussian component. (b) The component corresponding to the orthorhombic symmetry; and (c) the line shape corresponding to the tetragonal symmetry. Inset: the experimental spectrum and its fitting obtained using the extended Czjzek model ( $\eta = 0.8$ ,  $\varepsilon = 0.3$ , red line), and the line obtained with the model assuming that  $\eta = 0.0$  and  $\varepsilon = 0.3$ .

Analysis of the experimental spectra therefore indicates that the nanoparticles are stabilized predominantly in the o-phase, which can be clearly distinguished from the tetragonal line shape by the asymmetry parameter of the EFG.

### III. THEORETICAL MODELLING

#### A. Model Description

Elastic strains can induce ferroelectric state in  $\text{HfO}_2$  thin films [57, 58]. Recently, it has been shown theoretically that compressive chemical stress can induce the ferroelectric o-phase and related polar properties of spherical  $\text{HfO}_2$  nanoparticles [59]. Similar effects can be expected in the oxygen-deficient  $\text{Hf}_{0.5}\text{Zr}_{0.5}\text{O}_2$  nanoparticles considered in this work. This expectation is based on the fact that oxygen vacancies can induce strong chemical strains in oxide ferroelectrics [60, 61].

To study a possibility theoretically, let us consider an assemble of  $\text{Hf}_{0.5}\text{Zr}_{0.5}\text{O}_2$  core-shell nanoparticles with a quasi-spherical shape and narrow size distribution. Namely, the average size  $2R \approx 7$

nm and dispersion of sizes  $\delta \approx 0.5$  nm can be taken from TEM results. The cores are assumed to be defect-free, crystalline and insulating. The core is covered with a thin shell, whose thickness  $\Delta R$  is much smaller than the core radius  $R_c$  (see **Fig. 7**). The shell is assumed to be semiconducting due to the high concentration of oxygen vacancies, which can be ionized. Both neutral and ionized vacancies act as elastic defects, which induce strong chemical strains with a magnitude  $w_s$ . These strains are proportional to the product of Vegard strain  $W_s$  and the defect concentration  $n$ , namely  $w_s \cong W_s n$ . The absolute value of  $|W_s|$  (other name is “elastic dipole”) is about  $3 - 30 \text{ \AA}^3$  in oxide ferroelectrics [60, 61]. Therefore, the estimation  $n \approx (0.3 - 3) \cdot 10^{27} \text{ m}^{-3}$  for the atomic concentration  $n_0 \cong 6 \cdot 10^{28} \text{ m}^{-3}$  agrees with relevant experiments [62, 63, 64], which demonstrate that the defect concentration can exceed  $0.5 - 5 \%$  near the surface of various oxides, and corresponding chemical strains  $w_s$  can reach several percents. Due to the elastic mismatch at the core-shell interface, the chemical strains induce elastic stress in the core [59]. Nanoparticles are placed in a dielectric medium, which effective dielectric permittivity  $\epsilon_{eff}$  depends on their concentration. Following Ref.[59], we assume that the effective screening length  $\lambda_{eff}$  in the shell depends on the defect concentration  $n$  as  $\lambda_{eff} = \sqrt{\frac{\epsilon_0 k_B T}{2e^2 n \epsilon_{eff}}}$ , where  $\epsilon_0$  is the vacuum dielectric constant,  $k_B$  is the Boltzmann constant,  $T$  is the absolute temperature and  $e$  is the elementary charge.

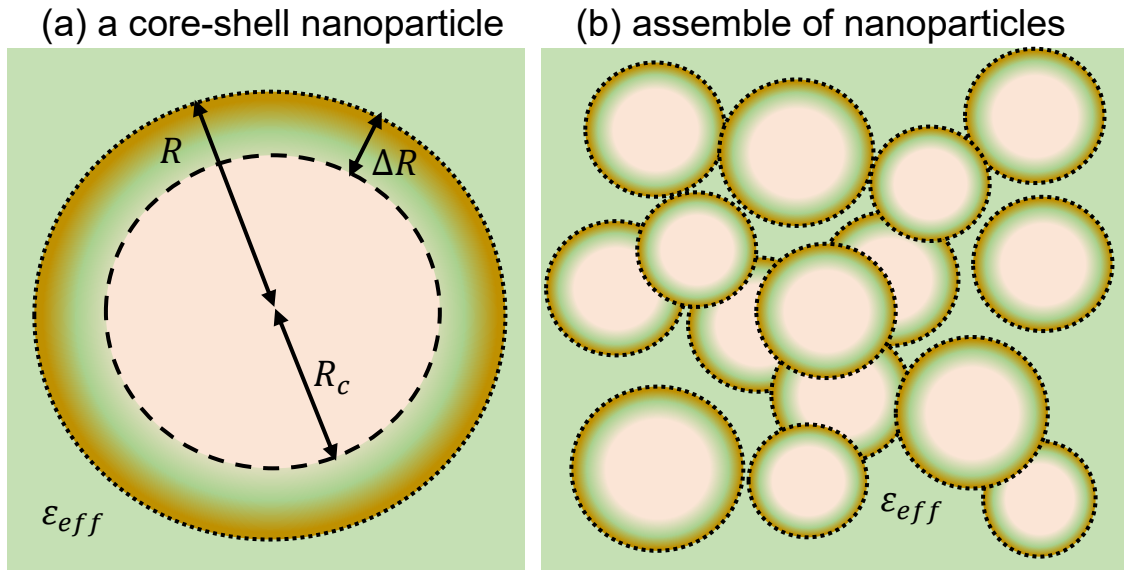


**Figure 7.** (a) The cross-section of a spherical  $\text{Hf}_{0.5}\text{Zr}_{0.5}\text{O}_2$  core-shell nanoparticle: a defect-free core of radius  $R_c$  is covered with a paraelectric shell of thickness  $\Delta R$ , which is full of elastic defects (oxygen vacancies) and free charges. (b) Assembly of the  $\text{Hf}_{0.5}\text{Zr}_{0.5}\text{O}_2$  core-shell nanoparticles with effective dielectric permittivity  $\epsilon_{eff}$ . The part (a) is adapted from Ref. [59].

To describe the phase diagrams of the  $\text{Hf}_{0.5}\text{Zr}_{0.5}\text{O}_2$  nanoparticles, we use the Landau-Ginzburg-Devonshire (LGD) approach proposed in Ref. [59]. The form of the free energy functional is based on

Delodovici et al. works [65, 66], and Jung and Birol works [67, 68], where the principal role of the trilinear coupling between the polar, antipolar and nonpolar modes has been established. The LGD free energy of the  $\text{Hf}_{0.5}\text{Zr}_{0.5}\text{O}_2$  nanoparticle core, corresponding to the ferroelectric o-phase, consists of the bulk energy density  $f_{bulk}$ , electric energy  $f_{el}$  and the surface energy  $F_s$  [59]:

$$F_{o-phase} = \int (f_{bulk} + f_{el})dV + F_s, \quad f_{bulk} = f_{bq} + f_{tr} + f_{est} + f_{grad}. \quad (3)$$

The bulk energy density  $f_{bulk}$  is the sum of the biquadratic energy  $f_{bq}$  and trilinear coupling energy  $f_{tr}$  of the polar, antipolar and nonpolar order parameters, elastic and striction energy contributions  $f_{est}$ , and the gradient energy of the order parameters  $f_{grad}$ . The energy  $f_{bq}$  is an expansion over the even powers and  $f_{tr}$  is an expansion over the odd powers of the dimensionless amplitudes  $Q_{\Gamma_3}$ ,  $Q_{Y_2}$  and  $Q_{Y_4}$  of the polar phonon mode  $\Gamma_{3-}$ , nonpolar phonon mode  $Y_{2+}$  and antipolar phonon mode  $Y_{4-}$  (see Refs.[57, 65, 66, 67, 68] for details). The energies  $f_{bq}$ ,  $f_{tr}$ ,  $f_{est}$ ,  $f_{grad}$  and  $f_{el}$  are listed in Refs. [59]. Corresponding material parameters are listed in Ref. [19]. Assuming the natural boundary conditions at the core-shell interface, namely  $\frac{\partial Q_i}{\partial \vec{n}} = 0$ , the surface energy  $F_s$  can be neglected in Eq.(3). Following the argumentation given in Refs.[57, 66], we consider the nonpolar tetragonal phase as the parent phase of the  $\text{Hf}_{0.5}\text{Zr}_{0.5}\text{O}_2$  core.

The polarization  $P_3$  is proportional to the amplitude  $Q_{\Gamma_3}$  of the  $\Gamma_{3-}$  mode [57, 66, 67]:

$$P_3 = \frac{Z_B^* d}{V_{f.u.}} Q_{\Gamma_3} \approx P_0 Q_{\Gamma_3}, \quad (4)$$

where the polarization amplitude  $P_0 \approx 54.8 \mu\text{C}/\text{cm}^2$  at room temperature [66].

The ferroelectric state of the core can be stable when its free energy  $F_{o-phase}$  is smaller than the energy of the m-phase,  $F_m = \int f_m dV$ , where  $f_m$  is the energy density of the m-phase in a bulk  $\text{Hf}_{0.5}\text{Zr}_{0.5}\text{O}_2$ .

## B. Theoretical Results

The averaged spontaneous polarization  $\bar{P}_s$  and the antipolar order parameter  $\bar{Q}_{Y_{4s}}$  of the  $\text{Hf}_{0.5}\text{Zr}_{0.5}\text{O}_2$  nanoparticles as a function of defect concentration  $n$  and Vegard strain  $W_s$  are shown in **Figs. 8(a)** and **8(b)**, respectively. Color scales in **Figs. 8(a)** and **8(b)** are the absolute values of  $\bar{P}_s$  and  $\bar{Q}_{Y_{4s}}$  in the deepest potential well of the free energy (3). The sharp boundary between the ferroelectric o-phase (with  $\bar{P}_s > 0$  and  $\bar{Q}_{Y_{4s}} > 0$ ) and nonpolar m-phase (with  $\bar{P}_s = 0$  and  $\bar{Q}_{Y_{4s}} = 0$ ) is the first order phase transition curve describing the dependence of the critical Vegard strain  $W_{cr}$  on the defect concentration  $n$  at room temperature  $T = 293$  K. As it was shown in Refs.[19, 59], the difference of the antipolar and nonpolar order parameters,  $|\bar{Q}_{Y_{4s}}| - |\bar{Q}_{Y_{2s}}|$ , is very small due to the negligible anisotropy of the deepest potential well as a function of  $|\bar{Q}_{Y_{4s}}|$  and  $|\bar{Q}_{Y_{2s}}|$ . Therefore, the dependence of  $|\bar{Q}_{Y_{2s}}|$  versus  $n$  and  $W_s$  looks very similar to those of  $|\bar{Q}_{Y_{4s}}|$ , and so it is not shown in **Fig. 8**.

It is seen from **Fig. 8**, the ferroelectric o-phase can be stable at compressive chemical strains only, namely at  $W_s < W_{min}$ , where  $W_{min} \approx -(3 - 5) \text{ \AA}^3$  for  $\epsilon_{eff} = 10 - 30$  and  $2\bar{R} = 7 \text{ nm}$ . Note that the used values of  $\epsilon_{eff}$  agree with the experimentally measured values of the relative dielectric permittivity of the  $\text{Hf}_{0.5}\text{Zr}_{0.5}\text{O}_2$  nanopowders at high frequency [69]. The necessity to create compressive chemical strains to induce the ferroelectric o-phase in the oxygen-deficient  $\text{Hf}_{0.5}\text{Zr}_{0.5}\text{O}_2$  nanoparticles agrees with DFT results for compressed  $\text{HfO}_2$  thin films [57, 66]. The ferroelectric o-phase is stable at defect concentrations  $n > n_{min}$ . The minimal concentration of defects,  $n_{min}$ , decreases with increase in  $\epsilon_{eff}$  from 1.2 % at  $\epsilon_{eff} = 10$  to 0.8 % at  $\epsilon_{eff} = 30$ . The region of the nonpolar m-phase stability decreases strongly with increase in  $n$ , being replaced by the ferroelectric o-phase. The decrease of the m-phase stability region and the minimal concentration  $n_{min}$  is explained by the increase of dielectric and space-charge screening emerging with increase in  $\epsilon_{eff}$  [57, 59].

The activation field  $E_{af}$  of polarization reversal can be estimated as  $E_{af} \cong b_{af}/\bar{P}_s$ , where  $b_{af}$  is the lowest barrier of polarization switching corresponding to the energy of the *Ccce* phase counted from the tetragonal parent phase [57, 59]. The value of  $b_{af}$  is almost constant,  $b_{af} \cong 48 \text{ meV/f.u.}$ , and the average spontaneous polarization  $\bar{P}_s$  depends on the Vegard strain  $W_s$ , defect concentration  $n$ , nanoparticle radius  $R$  and shell thickness  $\Delta R$  [59]. Color maps of  $E_{af}$  as a function of  $W_s$  and  $n$  are shown in **Figs. 8(e)** and **8(f)**. They are calculated for two values of the effective permittivity  $\epsilon_{eff} = 10$  and 30. The values of  $E_{af}$  changes from 0.68 MV/cm (far from the o-m phase boundary) to 0.98 MV/cm (nearby the o-m phase boundary); being very close to the activation fields calculated by us earlier in  $\text{HfO}_2$  thin films [57] and nanoparticles [59]. These activation fields are lower than the coercive fields  $E_c \cong 1.05 - 1.35 \text{ MV/cm}$  observed experimentally in 10-nm thick  $\text{Hf}_{0.5}\text{Zr}_{0.5}\text{O}_2$  films [70], because the local nucleation of nanodomains emerging at  $E_{af}$  precedes the global polarization switching emerging at  $E_c$ . The region of the lowest  $E_{af}$  corresponds to the largest  $n$  and  $W_s$ , because the compressive chemical stress is largest in the region. The region of the lowest  $E_{af}$  increases with increase in  $\epsilon_{eff}$  due to depolarization field decrease [59].

Color maps of the linear relative dielectric permittivity  $\epsilon_{33}$  as a function of  $W_c$  and  $n$  are shown in **Figs. 8(g) – 8(h)**, which are calculated for  $\epsilon_{eff} = 10$  and 30. As can be seen from the figure, the magnitude of  $\epsilon_{33}$  can be tuned by the choice of  $W_c$  and  $n$  from 10 to 35 at room temperature. The permittivity reaches maximal values (a little over 30) relatively far from the boundary between the o- and m-phases. The permittivity does not diverge at the o-m boundary, because the transition is of the first order. The region of maximal  $\epsilon_{33}$ , which has the shape of a wide curved stripe located relatively far from the boundary between the o- and m-phases, can be explained by the significant contribution of the nonpolar and antipolar orders to the permittivity due to the trilinear coupling in the free energy (3).

Otherwise, the permittivity should be maximal at the o-m boundary, that is not the case shown in **Figs. 8(g) – 8(h)**.

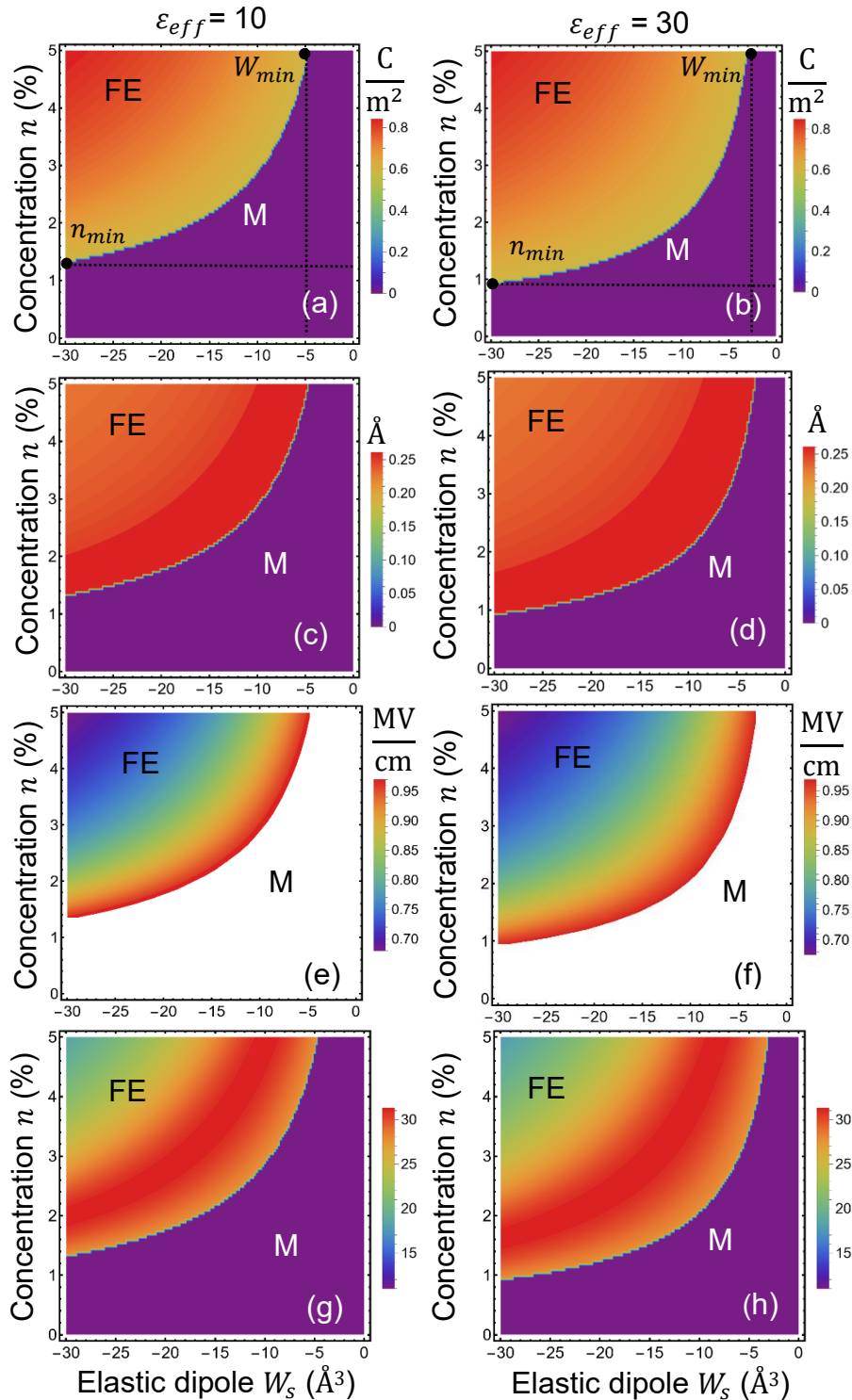


**Figure 8.** The absolute value of the spontaneous polarization  $\bar{P}_s$  (**a**, **b**), the amplitude of the antipolar order parameter  $|\bar{Q}_{Y4s}|$  (**c**, **d**), the activation field  $E_{af}$  (**e**, **f**), and the local dielectric permittivity of the core  $\epsilon_c$  (**g**, **h**) as a function of Vegard strain  $W_s$  and defect concentration  $n$  calculated for effective permittivity  $\epsilon_{eff} = 10$  (**a**, **c**, **e**, **g**) and 30 (**b**, **d**, **f**, **h**). Abbreviation “FE” is the FE o-phase, “M” denotes the nonpolar m-phase of the  $\text{Hf}_{0.5}\text{Zr}_{0.5}\text{O}_2$  nanoparticles. The average size of the nanoparticles is  $2\bar{R} = 7$  nm, shell thickness  $\Delta R = 1.5$  nm and  $T = 293$  K.

Material parameters used in calculations are listed in **Tables S1-S2** in **Appendix S1** of Ref. [57].

The calculated values of  $\epsilon_{33} \approx 10 - 30$  agrees well with the values of effective permittivity measured at 100 – 500 kHz in the densely pressed oxygen-deficient  $\text{Hf}_x\text{Zr}_{1-x}\text{O}_{2-y}$  nanopowders ( $x = 1, 0.6, 0.5$  and  $0.4$ ) with the 7 – 10 nm size of the particles [69]. Notably, that the nanoparticles, studied in Ref. [69], were annealed in the  $\text{CO}+\text{CO}_2$  ambient to induce the maximal amount of oxygen vacancies near the surface. Thus, calculated values of  $\epsilon_{33}$  is of the same order of magnitude as experimentally measured permittivity, being physically consistent with experimental results [69].

### C. Comparison with Experiment

Finally, let us relate the calculated values of  $\epsilon_{33}$  with the measured effective permittivity  $\epsilon_{eff}$  of the  $\text{Hf}_{0.5}\text{Zr}_{0.5}\text{O}_2 - \text{PVDF}$  nanocomposites, which contain  $\mu = 12.5$  vol. % of  $\text{Hf}_{0.5}\text{Zr}_{0.5}\text{O}_2$  nanoparticles. Temperature dependences of the effective dielectric permittivity of the  $\text{Hf}_{0.5}\text{Zr}_{0.5}\text{O}_2 - \text{PVDF}$  nanocomposites measured in the frequency range from 250 Hz to 1 MHz are shown in **Fig. 9**. The  $\text{Hf}_{0.5}\text{Zr}_{0.5}\text{O}_2$  nanopowders, used for the nanocomposite preparation, were annealed in air (their permittivity is smaller and shown in **Fig. 9(a)**) and in the  $\text{CO}+\text{CO}_2$  ambient (their permittivity is larger and shown in **Fig. 9(b)**). At low frequencies, the temperature dependence of  $\epsilon_{eff}$  has two distinct maxima, located at approximately 350 K and 430 K. The relative intensity of the  $\epsilon_{eff}$  low temperature maximum increases substantially for higher oxygen vacancy concentration (compare **Fig. 9(a)** with **Fig. 9(b)**). The magnitude of  $\epsilon_{eff}$  decreases monotonically with increase in frequency. Both peaks of  $\epsilon_{eff}$  exhibit a pronounced dispersion in their intensity, decrease strongly and vanish with increase in frequency from 250 Hz to 1 MHz (only hardly visible flexions remain at the light green curves in **Fig. 9**).

Such behavior of  $\epsilon_{eff}$  is maybe attributed to the Maxwell-Wagner (MW) effect, which arises due to the formation of the volume charges at the interfaces between different materials (particles and polymer in the considered case). However, as it was shown in the works [71, 72], the MW-type of effective dielectric permittivity reaches colossal values (more than  $10^4$ ) at low frequencies. The colossal permittivity of nanograined ferroelectric ceramics [73], nanopowders [74] and/or nanocomposites is usually caused by mesoscopic inhomogeneities in electrical conductivity (mainly between grains/particles and their boundaries), known as the effect of internal barrier layer capacitance (IBLC), as well as by inhomogeneous layers between electrodes and the sample, known as the effect of surface barrier layer capacitance (SBLC). The IBLC and SBLS effects cause the colossal dielectric response at low frequencies if the conductivity of the material between grains/particles is significantly lower than the conductivity of the grains/particles. In this case, the percolation of components with low conductivity

occurs. The effect is described by the effective medium approach (EMA), discussed in Refs. [75, 76], as well as in the works of Petzelt et al. [77] and Richetsky et al. [78].

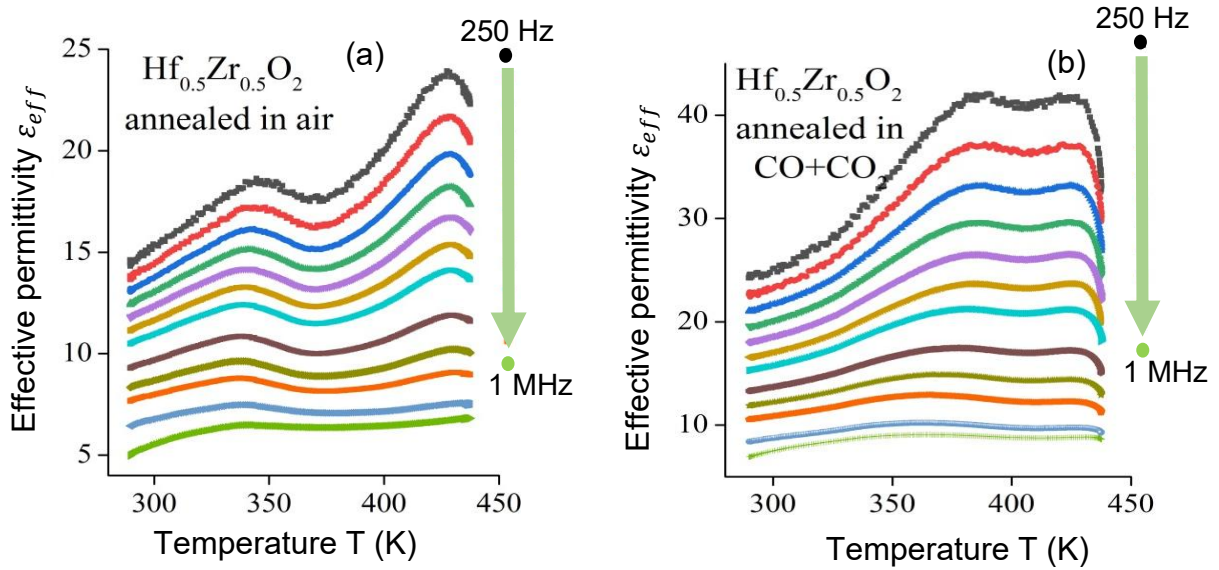


**Figure 9.** Temperature dependences of the effective dielectric permittivity of the  $\text{Hf}_{0.5}\text{Zr}_{0.5}\text{O}_2$  – PVDF nanocomposites measured in the frequency range from 250 Hz (top black curves) to 1 MHz (bottom light-green curves). The  $\text{Hf}_{0.5}\text{Zr}_{0.5}\text{O}_2$  nanopowders, used for the nanocomposite preparation, were annealed in air **(a)** and in the  $\text{CO}+\text{CO}_2$  ambient **(b)**.

However, the colossal dielectric permittivity was not observed experimentally in our case. Namely, the maximal value of  $\epsilon_{eff}$  is about 23 in **Fig. 9(a)** and does not exceed 45 in **Fig. 9(b)**. Using the EMA approach, below we estimate possible contributions of effects, related to the Maxwell-Wagner nature and to the ferroelectric-like dipolar nature, to the effective dielectric permittivity.

The dielectric permittivity of the pure PVDF varies from 10 – 12 (at low frequencies) to 7 – 5 (at high frequencies). The minimal value of  $\epsilon_{eff} \approx 15$  measured at the lowest frequency 250 Hz and room temperature for the sample N1 (annealed in air) agrees with the linear mixture formula for the  $\epsilon_{eff}$  at  $\mu = 12.5$  vol. % of  $\text{Hf}_{0.5}\text{Zr}_{0.5}\text{O}_2$  nanoparticles. The maximal value of  $\epsilon_{eff} \approx 24$  measured at 250 Hz and 420 K for the sample N1 does not agree with the linear mixture formula for the  $\epsilon_{eff}$ . Also, the linear mixture formula does not explain the physical nature of the two maxima of  $\epsilon_{eff}$  observed at low frequencies in the sample N1. Both the minimal ( $\epsilon_{eff} \approx 25$ ) and maximal ( $\epsilon_{eff} \approx 43$ ) values of  $\epsilon_{eff}$  measured at 250 Hz for the sample N2 (annealed in  $\text{CO}+\text{CO}_2$ ) might agree with the Maxwell-Garnet or Bruggeman approximations [79] for  $\mu = 12.5$  vol. %, only if one assume large values of the nanoparticles permittivity  $\epsilon_{33} > 10^2 - 10^4$  (see **Supplement S2** for details). The values of  $\epsilon_{33} \sim 10^2 - 10^4$  are significantly larger than the calculated values shown in **Fig. 8**. The required increase of  $\epsilon_{33}$  may indicate

the appearance of the superparaelectric (SPE)-like state in the  $\text{Hf}_{0.5}\text{Zr}_{0.5}\text{O}_2$  nanoparticles annealed in  $\text{CO}+\text{CO}_2$ . The SPE-like state often precedes the negative capacitance (NC) states of the ferroelectric nanoparticles, which may exist in the “dense” fine-grained ceramics [80] and composites with the volume fraction of nanoparticles  $\mu > 0.1$  [81, 82].

Thus, the discrepancy between calculated and estimated values of  $\varepsilon_{33}$  could point out other reasons of the observed increase in  $\varepsilon_{eff}$ , including the superparaelectric-like (SPE-like) or negative capacitance (NC) states of the ferroelectric nanoparticles. A possible interplay of MW-type, IBLS and SBLS effects, dipolar polarization, SPE-like and NC states can be estimated within the EMA, that yields the algebraic equation for the determination of the complex permittivity  $\varepsilon_{eff}^*$  of effective medium [80]:

$$(1 - \mu) \frac{\varepsilon_{eff}^* - \varepsilon_p^*}{(1 - n_f)\varepsilon_{eff}^* + n_f \varepsilon_p^*} + \mu \frac{\varepsilon_{eff}^* - \varepsilon_f^*}{(1 - n_f)\varepsilon_{eff}^* + n_f \varepsilon_f^*} = 0. \quad (5)$$

Here  $\varepsilon_f^*$  is the complex relative permittivity of the polarized nanoparticles “ $f$ ”, which are regarded monodisperse and uniformly polarized [81, 82]. The real part of  $\varepsilon_f^*$  corresponds to the dielectric response of the particles. The imaginary part of  $\varepsilon_f^*$  corresponds to the losses due to their finite ionic conductivity, being responsible for the manifestation of the MW-type and SBLS effects.  $\varepsilon_p^*$  is the complex relative permittivity of the dielectric polymer “ $p$ ”. The values  $\mu$  and  $1 - \mu$  are relative volume fractions of the components “ $f$ ” and “ $p$ ”, respectively. The maximal value  $\mu_{max}$  is limited by the dense packing of the particles. In particular,  $\mu_{max} = \frac{\pi}{6} \approx 0.52$  for densely packed nanospheres of the same radius. The function  $n_f$  is the depolarization field factor of the polarized nanoparticles, which is determined by their shape and polarization orientation;  $0 \leq n_f \leq 1$ . Analytical expressions for  $n_f$  exist for uniformly polarized nanoparticles of ellipsoidal shape including nanowires, nanospheres and nanodisks [83].

The solution of Eq.(5) for identical spherical nanoparticles, which have the same depolarization factor  $n_f = 1/3$ , is the following:

$$\varepsilon_{eff}^{\pm} = \frac{1}{4} \varepsilon_p^* (2 - 3\mu) + \frac{1}{4} \varepsilon_f^* (3\mu - 1) \pm \frac{1}{4} \sqrt{[\varepsilon_p^* (2 - 3\mu) + \varepsilon_f^* (3\mu - 1)]^2 + 8\varepsilon_p^* \varepsilon_f^*}. \quad (6)$$

Since the composite with  $\text{Hf}_{0.5}\text{Zr}_{0.5}\text{O}_2$  nanoparticles is a part of a capacitor structure in the dielectric measurements, both signs before the radical in Eq.(6) do not contradict thermal equilibrium. Since the sign “+” corresponds to higher value of effective permittivity, and we will consider this sign as those corresponding to the deepest energy minimum. Equation (6) is consistent with the linear mixture law only at  $\mu \ll 0.1$ ; deviations from the law become significant with increase in  $\mu$ .

It is possible to extract the temperature dependence of  $\varepsilon_f^*$  from Eq.(5), which has a relatively simple form at  $n_f = 1/3$ :

$$\varepsilon_f^* = \varepsilon_{eff}^* \frac{\mu [2\varepsilon_{eff}^* + \varepsilon_p^*] + 2(1 - \mu)(\varepsilon_{eff}^* - \varepsilon_p^*)}{\mu [2\varepsilon_{eff}^* + \varepsilon_p^*] - (1 - \mu)(\varepsilon_{eff}^* - \varepsilon_p^*)}. \quad (7)$$

Considering that  $\varepsilon_p^*$  is a real value, which decreases monotonically from 12 to 5 with increase in frequency, and  $\mu \approx 0.125$  in Eq.(7), the contribution of dipole polarization appears significant in the composite with  $\text{Hf}_{0.5}\text{Zr}_{0.5}\text{O}_2$  nanoparticles annealed in the  $\text{CO}+\text{CO}_2$  ambient. Consequently, the increase in the intensity of the dielectric permittivity peak, observed near 350 K in the PVDF film with the nanoparticles, can be related to the increase in oxygen vacancies concentration. The vacancies lead to the defect-induced elastic dipole formation and to the increase in ionic conductivity, which decreases the depolarization field (due to the decrease in the effective screening length  $\lambda_{eff}$ ) and may induce the SPE-like phase transition in the vacancy-enriched  $\text{Hf}_{0.5}\text{Zr}_{0.5}\text{O}_2$  nanoparticles.

#### IV. CONCLUSIONS

In this work we study the stabilization of the o-phase in small  $\text{Hf}_{0.5}\text{Zr}_{0.5}\text{O}_2$  nanoparticles (the average size 7 nm) annealed in air and in the  $\text{CO}+\text{CO}_2$  ambient. Concentration of the oxygen vacancies, which is determined by annealing conditions, was estimated as high as 10 – 15 % from the electron paramagnetic resonance spectra and X-ray photoelectron spectroscopy. The fraction of the orthorhombic phase that was controlled by the X-ray diffraction and nuclear magnetic resonance, depends on the concentration of oxygen vacancies, which are defined by annealing conditions.

Phenomenological calculations based on Landau-Ginzburg-Devonshire theory confirm that the chemical strains induced by oxygen vacancies can stabilize the orthorhombic phase with polar and antipolar long-range ordering in small hafnia-zirconia nanoparticles. We predict that the ferroelectric o-phase can be stable in small  $\text{Hf}_{0.5}\text{Zr}_{0.5}\text{O}_2$  nanoparticles at compressive chemical strains exceeding 1 – 5 % in the shell, which is well below the value 10 – 15 % estimated from XPS.

The contribution of dipole polarization was confirmed in the vacancy-enriched  $\text{Hf}_{0.5}\text{Zr}_{0.5}\text{O}_2$  nanoparticles. Consequently, the increase in the intensity of the dielectric permittivity peak, observed near 350 K in the PVDF film with the  $\text{Hf}_{0.5}\text{Zr}_{0.5}\text{O}_2$  nanoparticles annealed in the  $\text{CO}+\text{CO}_2$  ambient, is clearly associated with the increase in oxygen vacancies concentration. The vacancies lead to the defect-induced elastic dipole formation and to the increase in ionic conductivity, which decreases the depolarization field and may induce the SPE-like phase transition in the vacancy-enriched  $\text{Hf}_{0.5}\text{Zr}_{0.5}\text{O}_2$  nanoparticles.

#### Authors' contribution

Y.O.Z. measured the EPR and NMR spectra, analyzed them, analyzed XPS results and wrote the draft of experimental part of the work and SI. L.D. performed TEM, EDS and EELS studies. V.V.L., P.J., and J.H. performed XPS measurement and evaluation. O.V.L. and V.N.P. sintered the  $\text{Hf}_x\text{Zr}_{1-x}\text{O}_2$  nanopowders. A.O.D., M.D.V. and M.P.T. performed dielectric measurements. M.V.K. performed XRD studies. E.A.E. performed numerical calculations and prepared corresponding figures. A.N.M. performed

analytical calculations and wrote theoretical part of the work. All co-authors discussed and analyzed the results, and corresponding authors made all improvements in the manuscript.

### Acknowledgments

The work of Y.O.Z., L.P.Y., A.O.D., M.D.V. and E.A.E. is funded by the National Research Foundation of Ukraine (grant N 2023.03/0127 “Silicon-compatible ferroelectric nanocomposites for electronics and sensors”). P.J. and J.H. acknowledge the support of the Strategy AV21 project: “Study of the atomically thin quantum materials by advanced microscopic/spectroscopic techniques applying machine learning”. L.D. acknowledges support from the Knut and Alice Wallenberg Foundation (grant no. 2018.0237) for TEM research. Results of theoretical modelling were visualized in Mathematica 14.0 [84]. A.N.M. acknowledge the support the EOARD project 9IOE063 (related STCU partner project is P751c) and (in the part of discussion and application of results) the National Research Foundation of Ukraine (grant N 2023.03/0132 “Manyfold-degenerated metastable states of spontaneous polarization in nanoferroics: theory, experiment and perspectives for digital nanoelectronics”) and the Horizon Europe Framework Programme (HORIZON-TMA-MSCA-SE), project № 101131229, Piezoelectricity in 2D-materials: materials, modeling, and applications (PIEZO 2D).

## SUPPLEMENTARY MATERIALS

### Supplement S1. Samples characterization and Dielectric Measurements

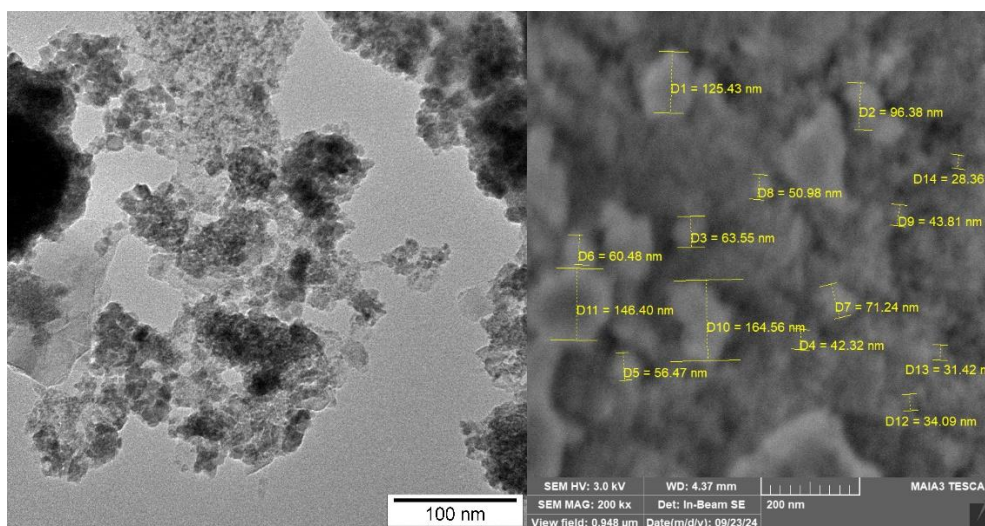


**Figure S1.** The TEM image (left) and the SEM image (right) of the sample N2.

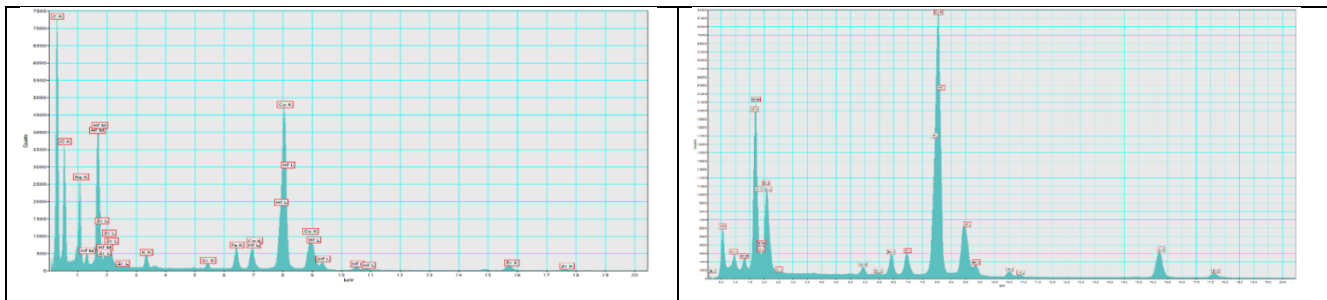


**Figure S2.** EDS spectra of the  $\text{Hf}_{0.5}\text{Zr}_{0.5}\text{O}_2$  samples annealed in air (left) and in  $\text{CO}+\text{CO}_2$  ambient (right).

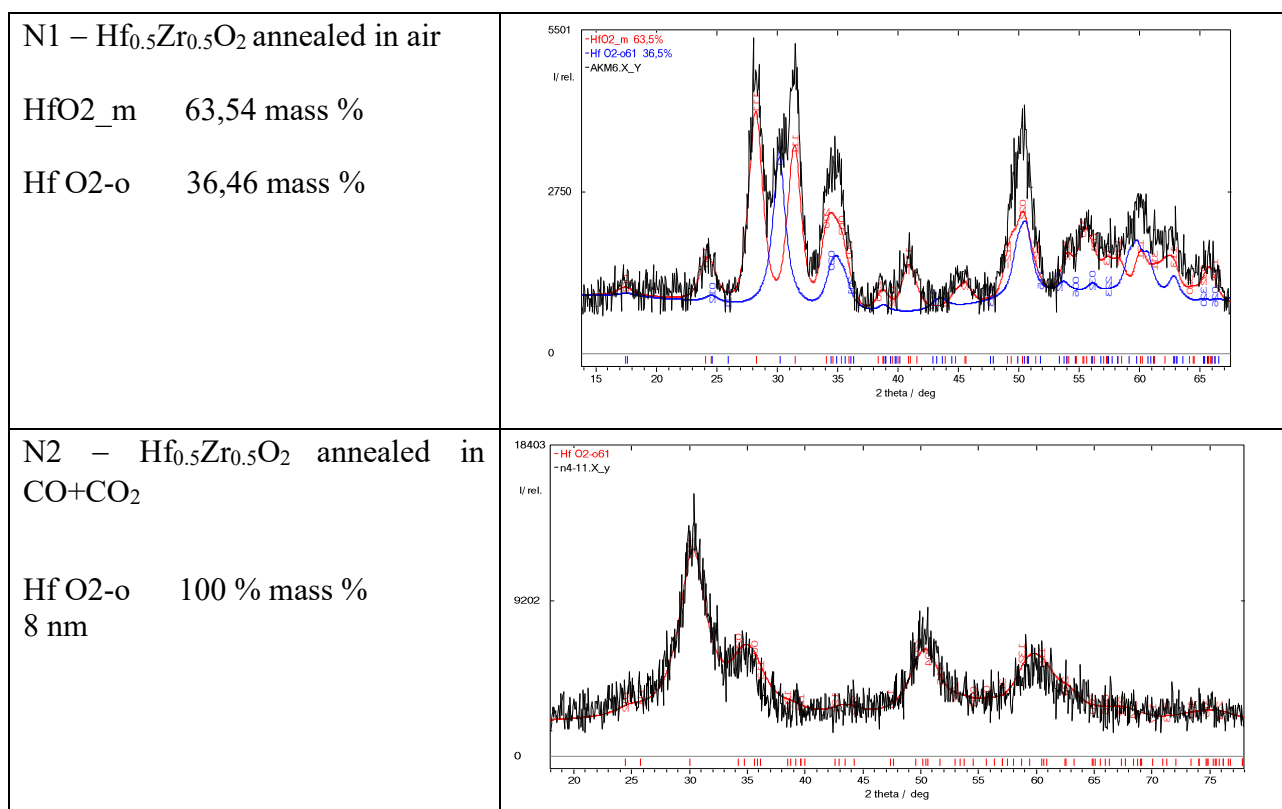


**Figure S3.** XRD spectra of the  $\text{Hf}_{0.5}\text{Zr}_{0.5}\text{O}_2$  nanoparticles annealed in air (a) and annealed in  $\text{CO}+\text{CO}_2$  ambient (b).

### Supplement S2. Dielectric measurements of nanocomposite “(Hf,Zr) $\text{O}_2$ nanoparticles – PVDF matrix”

The  $\text{Hf}_{0.5}\text{Zr}_{0.5}\text{O}_2$  powder occupied approximately 12.5 vol. % of the total composites volume. The concentration of nanoparticles in the PVDF was about 38.5 wt. % in the  $\text{Hf}_{0.5}\text{Zr}_{0.5}\text{O}_2$  samples annealed in  $\text{CO}+\text{CO}_2$  ambient, and about 39.4 wt. % in the  $\text{Hf}_{0.5}\text{Zr}_{0.5}\text{O}_2$  samples annealed in air. Effective dielectric permittivity of the  $\text{Hf}_{0.5}\text{Zr}_{0.5}\text{O}_2$  – PVDF nanocomposites is shown in Fig. S4.

In the Maxwell–Wagner case, dielectric constants often reach values on the order of tens of thousands at low frequencies, which was not observed in our experiment. At the same time, small dielectric permittivity  $\epsilon$  of PVDF ( $\approx 12$ ) complicates the determination of the true permittivity of the composite materials. The effective dielectric permittivity of the composite can be estimated by

Bruggeman's approach, which gives  $\varepsilon_{eff} = \frac{1}{4}(\beta + \sqrt{\beta^2 + 8\varepsilon_1\varepsilon_2})$ ,  $\beta = (3\eta_1 - 1)\varepsilon_1 + (3\eta_2 - 1)\varepsilon_2$ , where  $\eta_i$  represents the volume fraction of each constituent and  $\varepsilon_i$  corresponds to its dielectric constant. Thus, for a volume fraction of the  $\text{Hf}_{0.5}\text{Zr}_{0.5}\text{O}_2$  equal to 0.125, the effective dielectric permittivity ranges from about 16 to 19 when  $\varepsilon_{\text{HZO}}$  varies between 100 to 10000. It should be noted that applying the Bruggeman's model to experimental data does not yield meaningful dielectric constant values for the studied nanoparticles. This is likely due to the high conductivity of obtained composites and the tendency of nanoparticles to form irregular clusters, with possible air inclusions between the nanoparticles.

The solution of Eq.(5) for identical polarized nanoparticles, which have the same depolarization factor  $n_f$ , is the following:

$$\varepsilon_{eff}^{\pm} = \frac{(1-\mu)\varepsilon_p^* + \mu\varepsilon_f^* - n_f(\varepsilon_p^* + \varepsilon_f^*) \pm \sqrt{[(1-\mu)\varepsilon_p^* + \mu\varepsilon_f^* - n_f(\varepsilon_p^* + \varepsilon_f^*)]^2 + 4\varepsilon_p^*\varepsilon_f^*(1-n_f)n_f}}{2(1-n_f)}. \quad (\text{S.1})$$

Assuming that  $n_f = 1/3$ , we obtain from Eq.(S.1) that  $\varepsilon_{eff}^{\pm} = \frac{1}{4}\varepsilon_p^*(2 - 3\mu) + \frac{1}{4}\varepsilon_f^*(3\mu - 1) \pm \frac{1}{4}\sqrt{[\varepsilon_p^*(2 - 3\mu) + \varepsilon_f^*(3\mu - 1)]^2 + 8\varepsilon_p^*\varepsilon_f^*}$ .

It is possible to extract the temperature dependence of  $\varepsilon_f^*$  from Eq.(5) as:

$$\varepsilon_f^* = \varepsilon_{eff}^* \frac{\mu[(1-n_f)\varepsilon_{eff}^* + n_f\varepsilon_p^*] + (1-n_f)(1-\mu)(\varepsilon_{eff}^* - \varepsilon_p^*)}{\mu[(1-n_f)\varepsilon_{eff}^* + n_f\varepsilon_p^*] - n_f(1-\mu)(\varepsilon_{eff}^* - \varepsilon_p^*)}. \quad (\text{S.2})$$

Assuming that  $n_f = 1/3$ , we obtain from Eq.(S.2) that  $\varepsilon_f^* = \varepsilon_{eff}^* \frac{\mu[2\varepsilon_{eff}^* + \varepsilon_p^*] + 2(1-\mu)(\varepsilon_{eff}^* - \varepsilon_p^*)}{\mu[2\varepsilon_{eff}^* + \varepsilon_p^*] - (1-\mu)(\varepsilon_{eff}^* - \varepsilon_p^*)}$ .

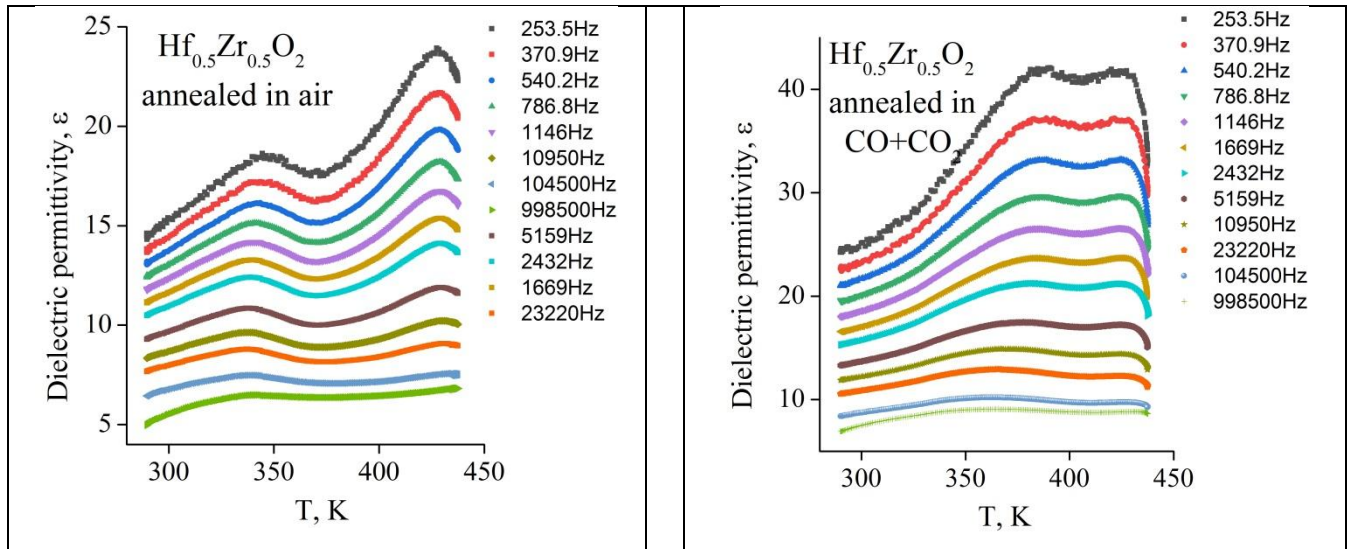


**Figure S4.** Effective dielectric permittivity of the  $\text{Hf}_{0.5}\text{Zr}_{0.5}\text{O}_2$  - PVDF nanocomposites. The  $\text{Hf}_{0.5}\text{Zr}_{0.5}\text{O}_2$  nanopowders, used for the nanocomposite preparation, were annealed in air (left) and in  $\text{CO}+\text{CO}_2$  ambient (right).

## References

- 
- [1] Johannes Müller, Tim S. Boscke, Uwe Schroder, Stefan Mueller, Dennis Brauhaus, Ulrich Bottger, Lothar Frey, and Thomas Mikolajic, “Ferroelectricity in Simple Binary ZrO<sub>2</sub> and HfO<sub>2</sub>”, *Nano Lett.* 2012, 12, 4318–4323, [dx.doi.org/10.1021/nl302049k](https://doi.org/10.1021/nl302049k)
- [2] T. S. Boscke, J. Muller, D. Brauhaus, U. Schroder, and U. Bottger, “Ferroelectricity in hafnium oxide thin films,” *Appl. Phys. Lett.* 99(10), 102903 (2011).
- [3] J. Muller, T. S. Boscke, D. Brauhaus, U. Schroder, U. Bottger, J. Sundqvist, P. Kucher, T. Mikolajick, and L. Frey, “Ferroelectric Zr<sub>0.5</sub>Hf<sub>0.5</sub>O<sub>2</sub> thin films for nonvolatile memory applications,” *Appl. Phys. Lett.* 99(11), 112901 (2011).
- [4] Roadmap on ferroelectric hafnia and zirconia-based materials and devices, *APL Mater.* **11**, 089201 (2023); <https://doi.org/10.1063/5.0148068>
- [5] K.-H. Kim, I. Karpov, R. H. Olsson III, D. Jariwala. Wurtzite and fluorite ferroelectric materials for electronic memory, *Nature Nanotechnology* **18**, 422 (2023); <https://doi.org/10.1038/s41565-023-01361-y>
- [6] A. Paul, G. Kumar, A. Das, G. Larrieu, and S. De. Hafnium oxide-based ferroelectric field effect transistors: From materials and reliability to applications in storage-class memory and in-memory computing. *J. Appl. Phys.* **138**, 010701 (2025); <https://doi.org/10.1063/5.0278057>
- [7] J. Wang, H. P. Li, and R. Stevens, “Hafnia and hafnia-toughened ceramics,” *J. Mater. Sci.* 27(20), 5397–5430 (1992); <https://doi.org/10.1007/BF00541601>
- [8] X. Luo, W. Zhou, S. Ushakov, A. Navrotsky, and A. Demkov, “Monoclinic to tetragonal transformations in hafnia and zirconia: A combined calorimetric and density functional study,” *Phys. Rev. B* 80(13), 134119 (2009); <https://doi.org/10.1103/PhysRevB.80.134119>
- [9] Y. Al-Khatatbeh, K. K. M. Lee, and B. Kiefer, “Phase diagram up to 105 GPa and mechanical strength of HfO<sub>2</sub>,” *Phys. Rev. B* 82(14), 144106 (2010), <https://doi.org/10.1103/PhysRevB.82.144106>
- [10] O. Ohtaka, H. Fukui, T. Kunisada et al., Phase relations and equations of state of ZrO<sub>2</sub> under high temperature and high pressure, *Phys. Rev. B* 63, 174108; <https://doi.org/10.1103/PhysRevB.63.174108>
- [11] Claudia Richter, Tony Schenk, Min Hyuk Park et al, Si Doped Hafnium Oxide—A “Fragile” Ferroelectric System, *Adv. Electron. Mater.* 2017, 3, 1700131, <https://doi.org/10.1002/aelm.201700131>
- [12] Shimizu, T., Katayama, K., Kiguchi, T. *et al.* The demonstration of significant ferroelectricity in epitaxial Y-doped HfO<sub>2</sub> film. *Sci Rep* 6, 32931 (2016); <https://doi.org/10.1038/srep32931>
- [13] Mueller, S. *etmal.* Incipient ferroelectricity in Al-doped HfO<sub>2</sub> thin films. *AdvancedmFunctionalMaterials.* 22, 2412-2417 (2012); <https://doi.org/10.1002/adfm.201103119>
- [14] S. Estandia, N. Dix, J. Gazquez, I. Fina, J. Lyu, M. F. Chisholm, J. Fontcuberta, and F. Sánchez, Engineering ferroelectric f<sub>0.5</sub>Zr<sub>0.5</sub>O<sub>2</sub> thin films by epitaxial stress, *ACS Appl. Electron. Mater.* **1**, 1449 (2019); <https://doi.org/10.1021/acsaelm.9b00256>

- 
- [15] S. Estandia, N. Dix, M. F. Chisholm, I. Fina, and F. Sánchez, Domain-matching epitaxy of ferroelectric Hf<sub>0.5</sub>Zr<sub>0.5</sub>O<sub>2</sub>(111) on La<sub>2/3</sub>Sr<sub>1/3</sub>MnO<sub>3</sub>(001), *Cryst. Growth Des.* **20**, 3801 (2020); <https://dx.doi.org/10.1021/acs.cgd.0c00095>
- [16] S. Zhou, J. Zhang, and A. M. Rappe. Strain-induced antipolar phase in hafnia stabilizes robust thin-film ferroelectricity. *Science Advances* **8** (47), eadd5953 (2022); <https://doi.org/10.1126/sciadv.add5953>
- [17] M. Pešić, F. P. G. Fengler, T. Schenk et. al., “Physical Mechanisms behind the Field-Cycling Behavior of HfO<sub>2</sub>-Based Ferroelectric Capacitors”, *Advanced Functional Materials*. **26**, 4601-4612 (2016). <https://doi.org/10.1002/adfm.201600590>
- [18] M. H. Park, Y. H. Lee, H. J. Kim, T. Schenk, W. Lee, K. Do Kim, F. P. G. Fengler, T. Mikolajick, U. Schroeder, and C. S. Hwang. Surface and grain boundary energy as the key enabler of ferroelectricity in nanoscale hafnia-zirconia: a comparison of model and experiment. *Nanoscale* **9**, 9973 (2017); <https://doi.org/10.1039/C7NR02121F>
- [19] A. N. Morozovska, E. A. Eliseev, S. V. Kalinin, and M. V. Strikha. Sizes of Ferroelectricity Appearance and Disappearance in Nanosized Hafnia-Zirconia: Landau-type Theory (2026); <https://doi.org/10.48550/arXiv.2601.06267>
- [20] Lim, S.; Ahn, Y.; Won, B.; Lee, S.; Park, H.; Kumar, M.; Seo, H. Effects of Substrate and Annealing Conditions on the Ferroelectric Properties of Non-Doped HfO<sub>2</sub> Deposited by RF Plasma Sputter. *Nanomaterials* **2024**, *14*, 1386. <https://doi.org/10.3390/nano14171386>
- [21] M. Hoffmann, U. Schroeder, T. Schenk et al., Stabilizing the ferroelectric phase in doped hafnium oxide, *J. Appl. Phys.* **118**, 072006 (2015); <https://doi.org/10.1063/1.4927805>
- [22] M. D. Glinchuk, A.N. Morozovska, A. Lukowiak, W. Stręk, M. V. Silibin, D. V. Karpinsky, Y. Kim, S. V. Kalinin, “Possible Electrochemical Origin of Ferroelectricity in HfO<sub>2</sub> Thin Films”, *Journal of Alloys and Compounds*, <https://doi.org/10.1016/j.jallcom.2019.153628>
- [23] E. A. Eliseev, Y. O. Zagorodniy, V. N. Pavlikov, O. V. Leshchenko, H. V. Shevilakova, M. V. Karpec, A. D. Yaremkevych, O. M. Fesenko, S. V. Kalinin, and A. N. Morozovska. Phase diagrams and polarization reversal in nanosized Hf<sub>x</sub>Zr<sub>1-x</sub>O<sub>2-y</sub>, *AIP Advances*, **14**, 055224 (2024); <https://doi.org/10.1063/5.0209123>
- [24] E. A. Eliseev, I. V. Kondakova, Y. O. Zagorodniy, H. V. Shevliakova, O. V. Leshchenko, V. N. Pavlikov, M. V. Karpets, L. P. Yurchenko, and A. N. Morozovska, The origin of the ferroelectric-like orthorhombic phase in oxygen-deficient HfO<sub>2-y</sub> nanoparticles. *Semiconductor Physics, Optoelectronics and Quantum Electronics*, **28**, 134 (2025); <https://doi.org/10.15407/spqeo28.02.134>
- [25] O. S. Pylypchuk, V. V. Vainberg, V. N. Poroshin, O. V. Leshchenko, V. N. Pavlikov, I. V. Kondakova, S. E. Ivanchenko, L. P. Yurchenko, L. Demchenko, A. O. Diachenko, M. V. Karpets, M. P. Trubitsyn, E. A. Eliseev, and A. N. Morozovska. A colossal dielectric response of Hf<sub>x</sub>Zr<sub>1-x</sub>O<sub>2</sub> nanoparticles. *Physical Review Materials* **9**, 114412 (2025); <https://doi.org/10.1103/y2pb-5g5w>
- [26] O. S. Pylypchuk, I. V. Fesych, V. V. Vainberg, Y. O. Zagorodniy, V. I. Styopkin, J. M. Gudenko, I. V. Kondakova, L. P. Yurchenko, V. N. Pavlikov, A. O. Diachenko, M. M. Koptiev, M. D. Volnyanskii, V. V. Laguta, E. A. Eliseev, M. P. Trubitsyn, and A. N. Morozovska. Resistive switching and charge accumulation in

---

Hf<sub>0.5</sub>Zr<sub>0.5</sub>O<sub>2</sub> nanoparticles. *Journal of Physical Chemistry* **29**, 31, 14299 (2025);

<https://doi.org/10.1021/acs.jpcc.5c04140>.

[27] E. A. Eliseev, Y. O. Zagorodniy, V. N. Pavlikov, O. V. Leshchenko, H. V. Shevilakova, M. V. Karpec, A. D. Yaremkevych, O. M. Fesenko, S. V. Kalinin, and A. N. Morozovska. Phase diagrams and polarization reversal in nanosized Hf<sub>x</sub>Zr<sub>1-x</sub>O<sub>2-y</sub>, *AIP Advances*, 14, 055224 (2024); <https://doi.org/10.1063/5.0209123>

[28] E. A. Eliseev, I. V. Kondakova, Y. O. Zagorodniy, H. V. Shevliakova, O. V. Leshchenko, V. N. Pavlikov, M. V. Karpets, L. P. Yurchenko, and A. N. Morozovska, The origin of the ferroelectric-like orthorhombic phase in oxygen-deficient HfO<sub>2-y</sub> nanoparticles. *Semiconductor Physics, Optoelectronics and Quantum Electronics*, 28 (2), 134-144 (2025); <https://doi.org/10.15407/spqeo28.02.134>

[29] R.R. Ernst, G. Bodenhausen, A. Wokaun, *Principles of Nuclear Magnetic Resonance in One and Two Dimensions*, Oxford university press, New York, 1990.

[30] Srivastava D.J., Giammar M., Venetos M.C., McCarthy-Carney L., and Grandinetti P.J. (2024) MRSimulator: A cross-platform, object-oriented software package for rapid solid-state NMR spectral simulation and analysis. *J. Chem. Phys.* 161, 212501, <https://doi.org/10.1063/5.0237608>

[31] Stoll, S.; Schweiger, A. EasySpin, a comprehensive software package for spectral simulation and analysis in EPR. *J. Magn. Reson.* 2006, 178 (1), 42.

[32] Konomi Fujimoto, *J Am Ceram Soc.* 2022;105:2823–2831, Orthorhombic-like atomic arrangement in hafnium-oxide-based nanoparticle, DOI: 10.1111/jace.18242

[33] R. Materlik, C. Küneth, and A. Kersch, *Journal of Applied Physics* 117, 134109 (2015); The origin of ferroelectricity in Hf<sub>1-x</sub>Zr<sub>x</sub>O<sub>2</sub> A computational investigation and a surface energy model, doi: 10.1063/1.4916707

[34] Mirengi, L.; Rizzo, A. An Accurate Quantitative X-ray Photoelectron Spectroscopy Study of Pure and Homogeneous ZrN Thin Films Deposited Using BPDMS. *Appl. Sci.* 2023, 13, 1271. <https://doi.org/10.3390/app13031271>

[35] G. Greczynski, D. Primetzhofer, J. Lu, L. Hultman, Core-level spectra and binding energies of transition metal nitrides by non-destructive x-ray photoelectron spectroscopy through capping layers, *Applied Surface Science*, Volume 396, 2017, Pages 347-358, <https://doi.org/10.1016/j.apsusc.2016.10.152>.

[36] Sarma D.D., Rao C.N.R.; *J. Electron Spectrosc. Relat. Phenom.* 20, 25; 1980; DOI: 10.1016/0368-2048(80)85003-1

[37] Ardizzone S., Cattania M.G., Lugo P.; *Electrochim. Acta* 39, 1509;1994; DOI: 10.1016/0013-4686(94)85128-X

[38] Lubna R Shah *et al*, 2009 *J. Phys.: Condens. Matter* 21 486004; DOI 10.1088/0953-8984/21/48/486004

[39] V. Grover *et al*, *Phys.Chem.Chem.Phys.*, 2014, 16,27065; DOI: 10.1039/c4cp04215h

[40] K. Wang, Y. Chang, L. Lv, Y. Long, Effect of annealing temperature on oxygen vacancy concentrations of nanocrystalline CeO<sub>2</sub> film, *Applied Surface Science* (2015), <http://dx.doi.org/10.1016/j.apsusc.2015.05.122>

[41] Chun-Yang Huang, *et al*, *Applied Physics Letters* 104, 062901 (2014); DOI: 10.1063/1.4864396

[42] Liu, H., Zheng, S., Chen, Q. *et al*. Structural and ferroelectric properties of Pr doped HfO<sub>2</sub> thin films fabricated by chemical solution method. *J Mater Sci: Mater Electron* 30, 5771–5779 (2019).

---

<https://doi.org/10.1007/s10854-019-00874-4>

[43] Rashid Mehmood *et al*, Surface, Subsurface, and Bulk Oxygen Vacancies Quantified by Decoupling and Deconvolution of the Defect Structure of Redox-Active Nanoceria, *Inorganic Chemistry* 2019 58 (9), 6016-6027, DOI: 10.1021/acs.inorgchem.9b00330

[44] H. Idriss, On the wrong assignment of the XPS O1s signal at 531–532 eV attributed to oxygen vacancies in photo- and electro-catalysts for water splitting and other materials applications, *Surface Science* 712 (2021) 121894, <https://doi.org/10.1016/j.susc.2021.121894>

[45] Alvaro Posada-Borbon *et al*, On the signatures of oxygen vacancies in O1s core level shifts, *Surface Science*, Volume 705, 2021, 121761; <https://doi.org/10.1016/j.susc.2020.121761>

[46] Kaihang Ye, Kunshan Li, Yirui Lu et al, An overview of advanced methods for the characterization of oxygen vacancies in materials, *TrAC Trends in Analytical Chemistry*, 116, 2019, 102-108; <https://doi.org/10.1016/j.trac.2019.05.002>.

[47] Qin Zhao, Xiping Wang, Tianxi Cai, The study of surface properties of ZrO<sub>2</sub>, *Applied Surface Science*, 225, Issues 1–4, 7-13 (2004); [https://doi.org/10.1016/S0169-4332\(03\)00832-8](https://doi.org/10.1016/S0169-4332(03)00832-8)

[48] Oleksandr S. Pylypchuk, Ihor V. Fesych, Victor V. Vainberg et al., Resistive Switching and Charge Accumulation in Hf<sub>0.5</sub>Zr<sub>0.5</sub>O<sub>2</sub> Nanoparticles, *The Journal of Physical Chemistry C* 2025 129 (31), 14299-14310, <https://doi.org/10.1021/acs.jpcc.5c04140>

[49] S. Wright, R.C. Barklie, EPR characterization of defects in monoclinic powders of ZrO<sub>2</sub> and HfO<sub>2</sub>, *Materials Science in Semiconductor Processing*, 9, Issue 6, 892-896 (2006);

[50] Qin Zhao, Xiping Wang, Tianxi Cai, The study of surface properties of ZrO<sub>2</sub>, *Applied Surface Science*, 225, Issues 1–4, 7-13 (2004); [https://doi.org/10.1016/S0169-4332\(03\)00832-8](https://doi.org/10.1016/S0169-4332(03)00832-8)

[51] Laguta, V. V., Elissalde, C., Maglione, M., Artemenko, A. M., Chlan, V., Štěpánková, H., & Zagorodniy, Yu. (2015). Crystal structure transformations induced by surface stresses in BaTiO<sub>3</sub> and BaTiO<sub>3</sub>@SiO<sub>2</sub> nanoparticles and ceramics. *Phase Transitions*, 88(8), 761–775. <https://doi.org/10.1080/01411594.2014.996852>

[52] T.J. Bastow, M.E. Smith, <sup>91</sup>Zr NMR characterisation of phases in transformation toughened zirconia, *Solid State Nucl. Magn. Reson.* (1992) 165-174

[53] Baugher, J. F.; Taylor, P. C.; Oja, T.; Bray, P. J. Nuclear magnetic resonance powder patterns in the presence of completely asymmetric quadrupole and chemical shift effects: application to mavanadates. *J. Chem. Phys.* 1969, 50, 4914–4925.

[54] T.J. Bastow, M.E. Smith, S.N. Stuart, Observation of <sup>91</sup>Zr NMR in zirconium-based metals and oxides, *Chemical Physics Letters*, Volume 191, Issues 1–2, 1992, 125-129, [https://doi.org/10.1016/0009-2614\(92\)85380-S](https://doi.org/10.1016/0009-2614(92)85380-S).

[55] Filipe Vasconcelos *et al*, Extended Czjzek model applied to NMR parameter distributions in sodium metaphosphate glass, 2013 *J. Phys.: Condens. Matter* 25 255402, [doi:10.1088/0953-8984/25/25/255402](https://doi.org/10.1088/0953-8984/25/25/255402)

[56] Gérard Le Caër *et al*, An extension of the Czjzek model for the distributions of electric field gradients in disordered solids and an application to NMR spectra of <sup>71</sup>Ga in chalcogenide glasses, 2010 *J. Phys.:*

- [57] S. Dutta, P. Buragohain, S. Glinsek, C. Richter, H. Aramberri, H. Lu, U. Schroeder, E. Defay, A. Gruverman, J. Íñiguez. Piezoelectricity in hafnia. *Nature Communications* 12, 7301 (2021); <https://doi.org/10.1038/s41467-021-27480-5>
- [58] S. Zhou, J. Zhang, A. M. Rappe, Strain-induced antipolar phase in hafnia stabilizes robust thin-film ferroelectricity. *Science Advances* 8 (47), eadd5953 (2022); <https://doi.org/10.1126/sciadv.add5953>
- [59] Anna N. Morozovska, Eugene A. Eliseev, Richard (Yu) Liu, Sergei V. Kalinin, and Dean R. Evans. Stress-Induced Ferroelectricity in Hafnium Oxide Core-Shell Nanoparticles (2026); <https://doi.org/10.48550/arXiv.2602.09262>
- [60] D. A. Freedman, D. Roundy, and T. A. Arias. Elastic effects of vacancies in strontium titanate: Short- and long-range strain fields, elastic dipole tensors, and chemical strain. *Phys. Rev. B* 80, 064108 (2009), <https://doi.org/10.1103/PhysRevB.80.064108>
- [61] Y. Kim, A. S. Disa, T. E. Babakol, and J. D. Brock. Strain screening by mobile oxygen vacancies in SrTiO<sub>3</sub>. *Appl. Phys. Lett.* 96, 251901 (2010), <https://doi.org/10.1063/1.3455157>
- [62] S. Bourgeois, B. Domenichini and J. Jupille, Excess Electrons at Oxide Surfaces, Chapter 4 in: *Defects at Oxide Surfaces*, ed.: J. Jupille and G. Thornton, Springer Series in Surface Sciences 58, (2015), [https://doi.org/10.1007/978-3-319-14367-5\\_4](https://doi.org/10.1007/978-3-319-14367-5_4)
- [63] M.J. Highland, T.T. Fister, D.D. Fong, P.H. Fuoss, C. Thompson, J.A. Eastman, S.K. Streiffer, and G.B. Stephenson. Equilibrium polarization of ultrathin PbTiO<sub>3</sub> with surface compensation controlled by oxygen partial pressure. *Phys. Rev. Lett.* 107, 187602 (2011). <https://doi.org/10.1103/PhysRevLett.107.187602>
- [64] S.M. Yang, A.N. Morozovska, R. Kumar, E.A. Eliseev, Y. Cao, L. Mazet, N. Balke, S. Jesse, R. Vasudevan, C. Dubourdieu, S.V. Kalinin. Mixed electrochemical-ferroelectric states in nanoscale ferroelectrics. *Nat. Phys.* 13, 812 (2017). <https://doi.org/10.1038/nphys4103>
- [65] F. Delodovici, P. Barone, and S. Picozzi. Finite-size effects on ferroelectricity in rhombohedral HfO<sub>2</sub>. *Phys. Rev. B* 106, 115438 (2022); <https://doi.org/10.1103/PhysRevB.106.115438>
- [66] F. Delodovici, P. Barone, and S. Picozzi, Trilinear-coupling-driven ferroelectricity in HfO<sub>2</sub>, *Physical Review Materials* 5, 064405 (2021); <https://doi.org/10.1103/PhysRevMaterials.5.064405>
- [67] S. Jung and T. Birol, Triggered ferroelectricity in HfO<sub>2</sub> from hybrid phonons, arXiv:2502.08633 (2025); <https://doi.org/10.48550/arXiv.2502.08633>
- [68] S. Jung and T. Birol, Electric Polarization from Nonpolar Phonons, arXiv: 2512.00628 (2025); <https://doi.org/10.48550/arXiv.2512.00628>
- [69] O. S. Pylypchuk, V. V. Vainberg, V. N. Poroshin, O. V. Leshchenko, V. N. Pavlikov, I. V. Kondakova, S. E. Ivanchenko, L. P. Yurchenko, L. Demchenko, A. O. Diachenko, M. V. Karpets, M. P. Trubitsyn, E. A. Eliseev, and A. N. Morozovska. A colossal dielectric response of Hf<sub>x</sub>Zr<sub>1-x</sub>O<sub>2</sub> nanoparticles. *Physical Review Materials* 9, 114412 (2025); <https://doi.org/10.1103/y2pb-5g5w>
- [70] H. S. Park, J. C. Shin, K. Do Kim, S. Jae Shin, J. Hee Song, S. Kyu Ryoo, I. Soo Lee, S. Hyun Lee, H. Nam, C. Seong Hwang. Enhancing ferroelectric properties of Hf<sub>0.5</sub>Zr<sub>0.5</sub>O<sub>2</sub> thin films using the HfN/TiN and

---

W/TiN bi-layer bottom electrodes. *Journal of Materiomics*, **11** (6), 101109 (2025);

<https://doi.org/10.1016/j.jmat.2025.101109>

[71] H. Han, D. Ghosh, J.L. Jones, & J. C. Nino, Colossal Permittivity in Microwave-Sintered Barium Titanate and Effect of Annealing on Dielectric Properties. *J. Am. Ceram. Soc.*, **96**, 485 (2013).

<https://doi.org/10.1111/jace.12051>

[72] J. Petzelt, D. Nuzhnyy, V. Bovtun, M. Savinov, M. Kempa, I. Rychetsky, Broadband dielectric and conductivity spectroscopy of inhomogeneous and composite conductors. *Phys. Stat. Sol. A* **210**, 2259 (2013),

<https://doi.org/10.1002/pssa.201329288>

[73] O. S. Pylypchuk, S. E. Ivanchenko, M. Y. Yeliseiev, A. S. Nikolenko, V. I. Styopkin, B. Pokhylko, V. Kushnir, D. O. Stetsenko, O. Bereznykov, O. V. Leschenko, E. A. Eliseev, V. N. Poroshin, N. V. Morozovsky, V. V. Vainberg, and A. N. Morozovska. Behavior of the Dielectric and Pyroelectric Responses of Ferroelectric Fine-Grained Ceramics. *Journal of the American Ceramic Society*, **108**, e20391 (2025);

<https://doi.org/10.1111/jace.20391>.

[74] O. S. Pylypchuk, V. V. Vainberg, V. N. Poroshin, O. V. Leshchenko, V. N. Pavlikov, I. V. Kondakova, S. E. Ivanchenko, L. P. Yurchenko, L. Demchenko, A. O. Diachenko, M. V. Karpets, M. P. Trubitsyn, E. A. Eliseev, and A. N. Morozovska. A colossal dielectric response of  $\text{Hf}_x\text{Zr}_{1-x}\text{O}_2$  nanoparticles. *Physical Review Materials* **9**, 114412 (2025); <https://doi.org/10.1103/y2pb-5g5w>

[75] M. Saleem, M. S. Butt, A. Maqbool, M. A. Umer, M. Shahid, F. Javaid, R. A. Malik, H. Jabbar, H. M. W. Khalil, L. D. Hwan, M. Kim, B.-K. Koo, S. J. Jeong, “Percolation phenomena of dielectric permittivity of a microwave-sintered  $\text{BaTiO}_3$ -Ag nanocomposite for high energy capacitor”, *Journal of Alloys and Compounds*, **822**, 153525 (2020), <https://doi.org/10.1016/j.jallcom.2019.153525>

[76] P. Lunkenheimer, S. Krohns, S. Riegg, S.G. Ebbinghaus, A. Reller, and A. Loidl, Colossal dielectric constants in transition-metal oxides. *Eur. Phys. J. Spec. Topics*, **180**, 61-89 (2009),

<https://doi.org/10.1140/epjst/e2010-01212-5>

[77] J. Petzelt, D. Nuzhnyy, V. Bovtun, D.A. Crandles. Origin of the colossal permittivity of (Nb<sup>+</sup> In) co-doped rutile ceramics by wide-range dielectric spectroscopy. *Phase Transitions* **91**, 932 (2018).

<https://doi.org/10.1080/01411594.2018.1501801>

[78] I. Rychetský, D. Nuzhnyy, J. Petzelt, Giant permittivity effects from the core-shell structure modeling of the dielectric spectra. *Ferroelectrics* **569**, 9 (2020). <https://doi.org/10.1080/00150193.2020.1791659>

[79] *Effective Medium Theory Principles and Applications*, Second Edition, TUCK C. CHOY, OXFORD University press, ISBN 978-0-19-870509-3

[80] O. S. Pylypchuk, S. E. Ivanchenko, M. Y. Yeliseiev, A. S. Nikolenko, V. I. Styopkin, B. Pokhylko, V. Kushnir, D. O. Stetsenko, O. Bereznykov, O. V. Leschenko, E. A. Eliseev, V. N. Poroshin, N. V. Morozovsky, V. V. Vainberg, and A. N. Morozovska. Behavior of the Dielectric and Pyroelectric Responses of Ferroelectric Fine-Grained Ceramics. *Journal of the American Ceramic Society*, **108**, e20391 (2025),

<https://doi.org/10.1111/jace.20391>.

[81] O. V. Bereznykov, O. S. Pylypchuk, V. I. Styopkin, S. E. Ivanchenko, D. O. Stetsenko, E. A. Eliseev, Z. Kutnjak, V. N. Poroshin, A. N. Morozovska, and N. V. Morozovsky. Interfacial Effects and Negative Capacitance

---

State in P(VDF-TrFE) Films with BaTiO<sub>3</sub> Nanoparticles. *Composites Interfaces* (2025);

<https://doi.org/10.1080/09276440.2025.2538943>

[<sup>82</sup>] A. N. Morozovska, O. V. Bereznykov, M. V. Strikha, O. S. Pylypchuk, Z. Kutnjak, E. A. Eliseev, and D. R. Evans. Domain Morphology, Electrocaloric Response, and Negative Capacitance States of Ferroelectric Nanowires Array. *Composite Interfaces* (2025); <https://doi.org/10.1080/09276440.2025.2605389>

[<sup>83</sup>] L.D. Landau, E.M. Lifshitz, L. P. Pitaevskii. *Electrodynamics of Continuous Media*, (Second Edition, Butterworth-Heinemann, Oxford, 1984).

[<sup>84</sup>] <https://www.wolfram.com/mathematica>,